

Radiation damage evolution in High Entropy Alloys (HEAs) caused by 3–5 MeV Au and 5 MeV Cu ions in a broad range of dpa in connection to mechanical properties and internal morphology

A. Mackova^{a,c,*}, V. Havránek^a, R. Mikšová^a, S. Fernandes^{a,b}, J. Matejicek^d, H. Hadraba^e, M. Vilemová^d, M.O. Liedke^f, J. Martan^g, M. Vronka^h, P. Haušildⁱ, M. Butterling^f, P. Honnerová^g, A.G. Attalah^f, A. Wagner^f, F. Lukac^d

^a Nuclear Physics Institute of the Czech Academy of Sciences, 250 68 Husinec – Řež, Czech Republic

^b Sorbonne Université, CNRS, Institut des NanoSciences de Paris, INSP, SAFIR, F-75005 Paris, France

^c Department of Physics, Faculty of Science, J.E. Purkinje University, České Mladeži 8, 400 96 Ústí nad Labem, Czech Republic

^d Institute of Plasma Physics of the Czech Academy of Sciences, Za Slovankou 3, 18200 Prague, Czech Republic

^e Institute of Physics of Materials of the Czech Academy of Sciences, Žižková 22, 61600 Brno, Czech Republic

^f Helmholtz-Zentrum Dresden – Rossendorf, Institute of Radiation Physics, Bautzner Landstraße 400, 01328 Dresden, Germany

^g New Technologies – Research Centre, University of West Bohemia, Univerzitní 8, 301 00 Plzeň, Czech Republic

^h FZU – Institute of Physics of the Czech Academy of Sciences, Na Slovance 1999/2, 18221 Prague, Czech Republic

ⁱ Czech Technical University in Prague, Faculty of Nuclear Sciences and Physical Engineering, Trojanova 13, 120 00 Prague, Czech Republic

ARTICLE INFO

ABSTRACT

Keywords:

High entropy alloys
Radiation hardness
Ion beam irradiation
Damage evolution
Fusion materials

High Entropy Alloys (HEAs) are prospective materials for nuclear fusion reactors and were irradiated in this study at a broad range of energetic ion fluences. Different ion masses (Cu and Au ions) and energies (3 and 5 MeV) were selected to investigate dpa (displacement per atom) development, radiation defect accumulation based on prevailing collision processes (Au ions) and ionization processes (Cu ions) in various HEAs. The studied HEAs differ in terms of elemental composition, internal morphology (grain structure) and other modifiers. Dpa values of 1 to ~66 were achieved at Cu and Au ion fluences from 4×10^{14} to 1.3×10^{16} ions.cm $^{-2}$ at room temperature, which generated varying levels of lattice damage. Theoretical simulations were performed to estimate the energy stopping and dpa depth distribution using SRIM code and compared with Au-concentration depth profiles determined by Rutherford backscattering spectrometry for Au-ions with 3 MeV ion energy. The prevailing energy losses of ions via ionization processes for Cu-5 MeV ions were found to increase the damage through lattice strain and probable lattice distortion, although the main defect introduction is expected to occur via collisions during nuclear stopping. Structural modification and defect accumulation were investigated by positron annihilation spectroscopy (PAS), which revealed a broader damaged layer with defects, where HEA-Nb (NbCrFeMnNi) exhibited the least damage accumulation from chosen alloys with no strong relation to the Au-5 MeV ion implantation fluence, whereas strong defect accumulation was recorded in the Au-ion implanted Eurofer97 used for comparison and HEA-Co (CoCrFeMnNi). PAS analysis also allowed defect sizes to be determined as an additional structural characteristic. The observed trends were also confirmed by thermal property analysis, with a worsening of thermal effusivity recorded after the irradiation in HEA-Co and Eurofer97. The worsening of the thermal properties was confirmed by the layer thickness, where the layer identified by PAS was found to be broader than the SRIM theoretical predictions. Nanoindentation measurements confirmed less pronounced radiation hardening of HEA-Nb relative to that observed in HEA-Co and Eurofer97. Transmission Electron Microscopy (TEM) analysis revealed layer thicknesses in reasonable agreement with the dpa depth profiles. The thermal effusivity decreased in the surface-irradiated layer in all investigated samples, the least influenced material was HEA-Nb.

* Corresponding author.

E-mail address: mackova@ujf.cas.cz (A. Mackova).

Introduction

Fusion reactor material technology is considered key to the successful realisation of fusion reactors [1,2]. Considerable neutron damage at rates of 3–4 dpa (displacement per atom)/year [3] and both transient and steady-state impacting plasma loads present risks to plasma-facing materials; accordingly, nuclear fusion-based power reactors require developments in terms of plasma-facing materials [4] to prevent degradation due to exposure to high temperatures, high-energy neutron fluxes and harsh environments, which can cause significant thermal and mechanical loads. High-entropy alloys (HEAs) have been proposed as structural materials in a variety of applications, from advanced nuclear reactors to superconductive materials [5–7]. The configurational entropy of mixing in multicomponent alloys tends to stabilise the solid solution based on simple underlying face-centred cubic (*fcc*) or body-centred cubic (*bcc*) crystal structures. HEAs exhibit high configurational entropy, which favours the formation of a solid solution rather than intermetallic compounds. These materials have attracted considerable research interest due to their wear resistance, corrosion resistance, high hardness, high ductility, excellent fatigue resistance, significant strength at both low and high temperatures [7] and good fracture toughness [8]. Many of these properties make HEAs potentially suitable for nuclear applications [13,14].

HEAs contain equimolar or near-equimolar principal element contents of 5–35 atomic %, in contrast to the intermetallic structure commonly found in conventional alloys [9–11]. Incorporating multiple principal elements allows a high-entropy solid solution to be developed with improved engineering characteristics [12]. Metals including Al, Cr, Fe, Co, Ni, Cu, Ti, V and Mn are commonly used in HEA systems [15–17]. The first HEA to be discovered was equimolar CoCrFeMnNi, often referred to as the Cantor alloy [18]. CoCrFeMnNi (HEA-Co) alloy has also been very widely investigated because of its attractive physical properties including cryogenic mechanical properties, thermodynamic stability and malleability [19,20]. Its microstructure consists of a single face-centred-cubic (*fcc*) solid solution.

An intensively studied strengthening method for HEAs is oxide dispersion strengthening, which is based on oxides including Al_2O_3 , TiO_2 , ZrO_2 and Y_2O_3 , which restrict dislocation motion by dispersion strengthening and restrain grains' growth due to the grain-pinning effect [8,21]. Because of its high hardness and thermal stability [22], Y_2O_3 is used as a dispersoid for oxide dispersion strengthening and can effectively strengthen HEA-Co. The use of this dispersoid leads to increased yield strength and reduced ductility, and the substantial yield strength increase can be attributed to dispersion strengthening, thus indicating the effectiveness of this strengthening method [8].

The use of refractory elements (W, Ti, Ta, Cr, V, Hf, Zr, Nb and Mo) to produce HEAs for high-temperature applications has become increasingly widespread, as this technique is an effective method for microstructural modification and property regulation. The addition of V to HEA-Co alloy was reported in [23], with the formation of an intermetallic sigma phase identified, resulting in enhanced microhardness and yield strength. The addition of Ti promoted secondary phase growth, which can play a positive role in improving yield strength [24].

Nb has a negative enthalpy of mixing with the constituent components in alloy [25], which favours the formation of secondary phases or intermetallic compounds in HEAs. Additionally, Nb has a larger radius (0.143 nm) than the five base elements (0.124–0.128 nm), which results in a substantial atomic size mismatch and lattice distortion. Accordingly, the characteristics of Nb have received extensive attention, and some research has demonstrated improved HEA mechanical properties following Nb addition. Due to nanocomposite formation in the presence of heavy solute elements such as Nb, the nanocomposite may result in increased hardness [26].

HEAs may also be particularly suitable for high-fluence irradiation applications because of their interpreted self-healing capabilities [27], which are assumed to relate to severe lattice distortions or atomic-level

stress caused by mismatches in atom size between the principal elements [28,29]. The irradiation damage caused in an alloy depends not only on the type of the incident particle (i.e. electron, neutron, proton or heavy ion) and its energy but also on the characteristics of the material being irradiated (e.g. atomic weight, bond strength, crystal structure, stacking fault energy, composition and microstructure) and the irradiation temperature [32]. Collisions between a neutron and an atom may result in the atom being displaced from its lattice site with considerable kinetic energy. This primary knock-on atom (PKA) possesses sufficient energy to then collide with and displace other atoms, which in turn collide with others, thus creating a displacement cascade. This process results in multiple displacements and the formation of corresponding Frenkel pairs (FPs), ultimately causing damage that results in other irradiation-induced damage phenomena. The resulting interstitials can diffuse to recombine with vacancies, be absorbed in sinks such as grain boundaries or accumulate in small clusters. In the long term, the movement of these FPs continues, leading to extended defect formation and long-range damage [32]. Ions lose their energy via ionisation (electronic stopping) and collisions with nuclei of irradiated targets (nuclear stopping). However, heavier ions with lower energies of several MeV are advantageous for analysis as the penetrating ions modify the near-subsurface layer less than 1 μm from the material's surface – such modified layers can be more readily investigated with surface analytical methods and sufficiently high dpa can be achieved with lower ion energies used for irradiation.

Compared to neutron irradiation, ion irradiation has several advantages, principally its ability to more rapidly achieve significant dpa and the lack of activation that complicates post-irradiation handling and investigation of neutron-irradiated materials [33,36]. In some cases, using significantly higher ion energies for implantation and radiation damage studies in plasma-facing materials is particularly advantageous to avoid the complications associated with low ion energy implantation (e.g. for nano-indentation and thermal transport measurements [34–35]).

Radiation damage accumulation, radiation tolerance and the corresponding thermal and mechanical properties were investigated in HEA-Nb alloy at various Au-ion fluences of 5 MeV energy to achieve a broad dpa range in this study. In addition, Cu ions of 5 MeV were used to compare the effects of radiation with much lighter ions of the same energy. We also selected the highest achievable dpa value to compare radiation tolerance and property modification in HEA-Nb, HEA-Co, HEA-Co + Y_2O_3 and Eurofer97. The influence of the composition of each in terms of damage accumulation, as well as the thermal and mechanical properties, was compared to conventional Eurofer 97 steel, the main candidate structural material for ITER and future fusion power plants [37].

In this study, we aimed to compare and gain deeper insights into the defect nature and accumulation in HEA-Co and NbCrFeMnNi (HEA-Nb), which were anticipated to differ due to the preliminarily studied HEA-Nb radiation hardness values reported in [26]. We used Au-ions of 3–5 MeV energy with various ion fluences to investigate defect accumulation scaling with ion fluence in HEAs, with damage saturation and radiation resistance behaviours expected at high ion fluences. In the case of HEA-Co, we did not investigate dpa scaling (only one ion fluence was used) as this HEA has previously been extensively studied [19,20]. We thus chose the highest Au-ion fluence and parameters to achieve the same dpa for both HEAs in the subsurface region. Eurofer97 was used as a reference material. Cu-ions were used to track defect accumulation for lighter ions, which lose energy via ionisation rather than collision processes. In the existing literature, He-ion irradiation, heavy ion irradiation or self-implantation (e.g. Ni/Fe into NiCoFeCr alloy) have primarily been used, with a particular focus on high ion fluences with dpa values above 100 to determine void creation and elemental and internal morphology changes in response to irradiation [30,31]. The response of HEA-Co and HEA-Co + Y_2O_3 to high fluence ion radiation is investigated in our study to assess the Y_2O_3 oxide dispersoid's role in defect

accumulation resulting in mechanical and thermal property modification following irradiation. HEA-Co samples with and without dispersoid were irradiated with Au-ions of 3 MeV energy and compared to Eurofer97.

Based on the above, the key objectives of this study were: i) assessing radiation damage accumulation for a wide range of dpa values from 1 to 66, which is rare in the literature; ii) investigating the defects created by these irradiation conditions, structural modification and internal morphology (microstructure) in the buried layer and beyond using Positron Annihilation Spectroscopy (PAS) and Transmission Electron Microscopy (TEM); and iii) determining the thermal transport properties and hardness as indirect consequences of radiation defect accumulation and dissipation after irradiation.

Experimental

Equiatomic CoCrFeMnNi and NbCrFeMnNi high entropy alloys (HEA-Co and HEA-Nb respectively) were prepared from pure elements (Sigma Aldrich, USA) using the mechanical alloying method. The 100 g blend of powders was mechanically alloyed using a planetary ball mill (Pulverisette P-6, Fritsch). The milling process was performed in a hardened steel vial with steel balls for 24 h under vacuum conditions. The oxide dispersion strengthened (ODS) variant of HEA-Co was prepared by adding O₂ gas and Y and Ti powders to the blend during mechanical alloying. Details of the preparation process are described in detail in our previous work [38]. The alloyed powders were compacted using the spark plasma sintering technique in a TT SPS 10-4 furnace (Thermal Technology LLC, USA) at a temperature of 1150 °C. The fully dense pellets with a diameter of 30 mm were then machined to a shape suitable for testing using electro-discharge machining; for details, see also [36]. Eurofer97 is considered the reference structural material for the first wall and blanket of the DEMO fusion reactor [37]. The HEA composition, density, sample notation and irradiation parameters are summarised in Table 1.

Ion irradiation and SRIM calculation

Ion irradiation of HEAs was performed with Au ions with an energy of 5 MeV (Au-5 MeV) from a Tandetron accelerator using an ion implantation instrument, which enabled a homogeneous distribution of ion fluence across the sample area. The Au-5 MeV ions are sufficiently heavy to introduce collision cascades and displacement within a layer suitable for many surface analytical methods; in addition, the nuclear stopping of these ions is large enough to achieve significant dpa. In contrast, the Cu-5 MeV ions are much lighter and introduce a more significant portion of energy via the ionisation processes (electronic stopping). The ionisation (electronic stopping S_e) versus nuclear stopping (S_n) ratio (S_e/S_n) has a

Table 1

HEA sample description, elemental composition and suggested volume density in addition to the ion-irradiation parameters (ion mass, ion charge state and ion energy and fluence).

Sample label	Composition	Density (g. cm ⁻³)	Ion irradiation Ion mass charge state/ energy (MeV)	Ion fluence (cm ⁻²)
HEA-Co	CoCrFeMnNi	7.75	Au ²⁺ /3 MeV	1 × 10 ¹⁶
HEA-Co + Y ₂ O ₃	CoCrFeMnNi + Y ₂ O ₃	7.75	Au ²⁺ /3 MeV	1 × 10 ¹⁶
HEA-Nb	NbCrFeMnNi	8.3	Au ²⁺ /5 MeV	1.3 × 10 ¹⁶
HEA-Nb	NbCrFeMnNi	8.3	Au ²⁺ /5 MeV	1.3 × 10 ¹⁵
HEA-Nb	NbCrFeMnNi	8.3	Au ²⁺ /5 MeV	5 × 10 ¹⁵
HEA-Nb	NbCrFeMnNi	8.3	Au ²⁺ /5 MeV	4 × 10 ¹⁴
HEA-Nb	NbCrFeMnNi	8.3	Cu ²⁺ /5 MeV	1 × 10 ¹⁶
Eurofer97	Fe (91 wt%) + Cr (9 wt%)	7.8	Au ²⁺ /3 MeV	1 × 10 ¹⁶

value of around 2 and 0.6 for Cu-5 MeV and Au-5 MeV ions, respectively. Thus, Au-5 MeV ions will achieve higher dpa production in a shallower sub-surface layer relative to Cu-5 MeV irradiation. The calculations of electronic and nuclear stopping caused by Au-3 MeV, Au-5 MeV and Cu-5 MeV ions were performed using SRIM software [39]. The ionisation and nuclear stopping values of the ions used in this study are presented for Au-5 MeV and Cu-5 MeV ions in HEA-Nb in Fig. 1a and b and for Au-3 MeV ions in HEA-Co in Fig. 1c. The SRIM simulation results are not presented for Eurofer97, as the energy stopping of Au-3 MeV ions in this material is very similar to that shown in Fig. 1c. The elemental compositions and densities of the irradiated materials and ion beam parameters implemented in the SRIM simulation were taken from Table 1.

The nuclear stopping determines the vacancy appearance throughout the depth range at which the dpa values have been calculated; the results of this analysis are presented in Table 2 and Fig. 1d.

Various Au-ion fluences were used to reach a broad range of radiation damage values to study the defect structure within a heavy-ion-damaged region. SRIM calculation also requires additional parameters such as the elemental displacement energies E_d for each matrix element, as presented in Table 2, based on existing data for various metals [41,42,43]. SRIM was used for the calculation of the projected range R_p of ions with the standard deviation ΔR_p assuming a constant threshold displacement energy for each of the elements, as listed in Table 2. Dpa values are influenced by the ion's mass and energy. Ion irradiation dpa values were derived using SRIM following the recommendations of Stoller (quick Kinchin-Pease calculation) [40].

Defect accumulation analysis using PAS and Au-depth profiling with RBS

Positron annihilation spectroscopy (PAS) is a powerful technique that provides unique information regarding open-volume lattice defects [44,45]. In this study, PAS investigations were performed using either fast positrons emitted by a ²²Na radioisotope or slow positrons obtained by moderation of fast positrons. Doppler broadening variable energy positron annihilation spectroscopy (DB-VEPAS) measurements were conducted using a ²²Na-based monoenergetic positron beam, which allows offline experiments. The DB-VEPAS measurements were conducted at the apparatus for in situ defect analysis (AIDA) [46] of the slow positron beamline (SPONSOR) [47]. Positrons were implanted into a sample with discrete kinetic energies E_p in the range of 0.05–35 keV, hence characterising a depth profile starting at the surface down to a depth of ~1 μm. A mean positron implantation depth z_{mean} was approximated using a simple material density (ρ) dependent formula [48]:

$$z_{\text{mean}} = \frac{3.6}{\rho} E_p^{1.62} \quad (1)$$

z_{mean} approximates the depth and is not an absolute measure since it does not account for positron diffusion. The best estimation is provided for materials with high defect concentrations and, hence, low positron diffusion lengths, as is the case here. The volume density ρ = 8 g·cm⁻³ was utilized for all the samples. Measurements of the specimens were performed at room temperature under vacuum pressures ≤ 2 × 10⁻⁷ mbar. Using DB-VEPAS, it was possible to access the relative changes of defect concentration induced by Au and Cu-ion irradiation across the implantation profile and beneath. Variable energy positron annihilation lifetime spectroscopy (VEPALS) measurements were conducted at the Mono-energetic Positron Source (MePS) beamline at HZDR, Germany [49,50]. A typical lifetime spectrum N(t), representing the absolute value of the time derivative of the positron decay spectrum, is described by:

$$N(t) = \sum_{i=1}^{k+1} \frac{I_i}{\tau_i} e^{\frac{-t}{\tau_i}} \quad (2)$$

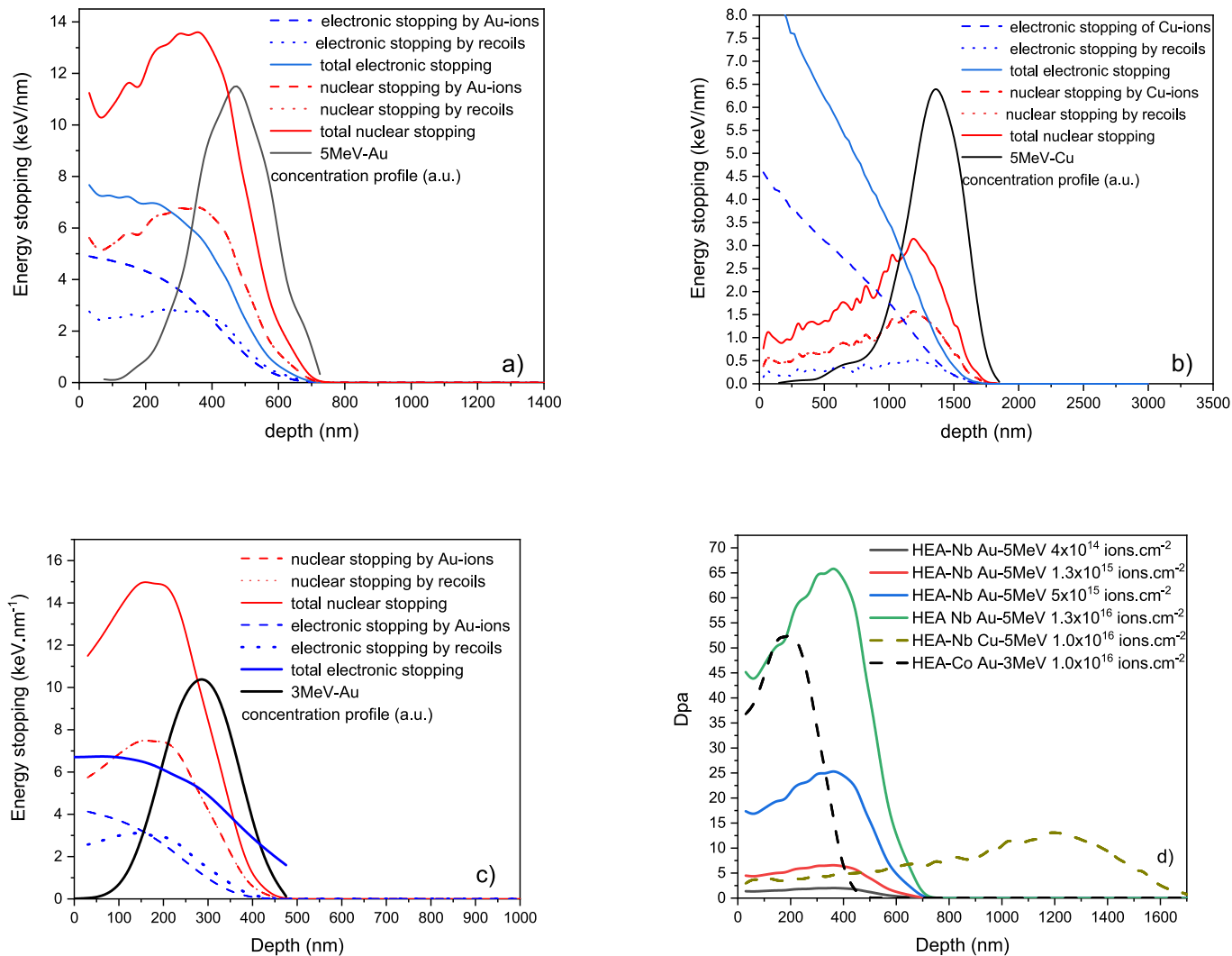


Fig. 1. SRIM simulations of energy stopping (ionisation and nuclear losses) generated by ions and recoils by a) Au-5 MeV ion irradiation in HEA-Nb, b) Cu-5 MeV ion irradiation in HEA-Nb and c) Au-3 MeV ions in HEA-Co based on the parameters from Table 1 and Table 2. The implanted ion depth profiles are also presented for each case showing the penetration depths of the appropriate ions. A comparison of the dpa depth profiles calculated based on SRIM-simulated data is presented in d) for all investigated samples except for HEA-Co + Y₂O₃ and Eurofer 97 due to the similarity with HEA-Co with the same ion irradiation parameters.

Table 2

Summary of the ion implantation parameters, including SRIM-calculated projected ranges R_p, dpa (maximal values), and displacement energies E_d.

Material	NbCrFeMnNi	Eurofer97	CoCrFeMnNi	
			CoCrFeMnNi	CoCrFeMnNi + Y ₂ O ₃
E _d (eV) (Fe, Cr, Co, Mn, Ni**)	40	40	40	40
E _d (eV) (Co, Nb**)	60	—	60	60
Projected range of Au-5 MeV ions	R _p = 461	—	—	—
Deviation of projected range (nm)	ΔR _p = 110	—	—	—
Projected range of Au-3 MeV ions	—	R _p = 281	R _p = 288	—
Deviation of projected range (nm)	—	ΔR _p = 70	ΔR _p = 73	—
Projected range of Cu-5 MeV ions	R _p = 1311	—	—	—
Deviation of projected range (nm)	ΔR _p = 240	—	—	—
Au-5 MeV ion fluence (ions.cm ⁻²) and corresponding dpa range**	1.3 × 10 ¹⁶ 5 × 10 ¹⁵ 1.3 × 10 ¹⁵ 4 × 10 ¹⁴	45–66 17–25 4–6 1–2	— — — —	— — — —
Cu-5 MeV ion fluence (ions.cm ⁻²) and corresponding dpa range**	1 × 10 ¹⁶	2–13	1 × 10 ¹⁶ 36–53	1 × 10 ¹⁶ 37–52

**dpa ranges calculated based on displacement energies [41,42] and SRIM calculation while adopting the approach published in [40].

where different defect types contributing to the positron trapping are related to $k+1$ components in the spectra with the individual lifetimes τ_i and intensities I_i ($\sum I_i = 1$) [44]. All the spectra were deconvoluted using

a non-linear least-squares fitting method within the fitting software package PALSfit [51] into two discrete lifetime components, which describe delocalized annihilation (bulk annihilation, τ_B) and localized

annihilation at a defect or direct localization at two different defect types (sizes; τ_1 and τ_2). The corresponding relative intensities largely reflect the concentration of each defect type (size) if the compared defects are within a similar size range. In general, positron lifetime is directly proportional to the defect size: the larger the open volume, the lower the annihilation probability and the longer it takes for positrons to be annihilated with electrons [52]. The positron lifetime and its intensity were determined as a function of positron implantation energy E_p or, effectively, the implantation depth (i.e. thickness).

Rutherford backscattering spectrometry (RBS) was used to determine the implanted Au-ion distribution in the selected cases, as RBS kinematics allow heavy implanted species in the matrix to be determined based on the depth of Au-ion incorporation. The backscattered He-ion yield was detected by RBS using a beam of 2.0 MeV He^+ ions from a Tandetron accelerator. The separated Au-signals in the recorded spectra allow depth profiling of Au-implanted specie to be achieved in the studied samples. An Ultra-Ortec PIPS detector recorded back-scattered He ions in a Cornell geometry with a laboratory scattering angle of 170°. The ion currents used during the RBS analysis were about 5nA and several RBS spectra were measured on different beam spots to reduce the effects of additional radiation damage introduction in the sample. A beam spot of around 1 mm² was used, and the final spectrum was obtained by summing the individual spectra.

Thermal effusivity and optical properties

The thermal effusivity at various depths below the sample surface was determined by a measurement system based on pulsed photothermal radiometry, as described in detail in [53,54]. This system uses a pulsed laser to heat the material surface and a fast infrared detector to observe the temperature decrease after the laser pulse impact. Based on the temperature decrease with time in the nanosecond time range, the thermal effusivity was evaluated at depths of hundreds of nanometres within the sample.

Thermal effusivity represents the square root of thermal conductivity, specific heat and density, and expresses a material's ability to exchange heat between its surroundings and itself at a surface. The experimentally measured effusivity evolution over time can be analysed and fitted to obtain the thermal conductivity. The thermal properties of surface layers are varied in the model until the temporal evolution of the calculated effusivity fits the experimentally determined values. The model is a three-layer 1D model with surface absorption of laser light and no thermal interface resistances between layers; the details of this model are published in [55].

The spectral normal hemispherical reflectivity was measured using a UV-VIS-NIR dispersion spectrophotometer (Specord 210 Plus) equipped with a commercial integrating sphere system with an incidence angle of 8° in the spectral range 320–1200 nm. First, a calibrated reflectivity standard with high reflectivity was placed on the sample port of the integrating sphere and a reference signal was measured. The reference standard was then replaced by a sample, and the corresponding sample signal was measured. The spectral normal hemispherical reflectivity was evaluated as the ratio of the measured signals multiplied by the reflectivity standard calibration curve. Based on the analysed reflectivity, the spectral normal absorptivity was calculated according to Kirchhoff's law [56] as a supplement to 1, assuming that the spectral normal hemispherical transmissivity was zero for the analysed samples. Subsequently, the absorptivity of a laser wavelength of 532 nm was read from the spectral waveforms for thermal effusivity evaluation.

X-ray diffraction

The microstructure changes in the irradiated materials are reflected in their X-ray diffraction (XRD) patterns, namely via diffraction-angle-dependent peak broadening. Typical changes observed in irradiated materials are decreases in crystallite size (coherently diffracting

domains) and increases in microstrain, e.g. as demonstrated in [57]. Therefore, XRD was performed on both pristine and irradiated samples using a Bruker D8 Discover diffractometer (Bruker AXS, Germany) with Cu radiation. The analysis of phase composition and microstructural parameters (crystalline size and microstrain) was conducted by Rietveld refinement of the full XRD patterns using TOPAS V5 software (Bruker AXS, Germany). The small crystallites and microstrains were assumed to contribute to the broadening of the Lorentzian and Gaussian components of the pseudo-Voigt function, respectively [58].

Mechanical properties – Nano-indentation

The measurements were performed on an Anton Paar NHT² nano-indenter with a Berkovich indenter by successive loading and unloading (continuous multi-cycle method; CMC). The CMC loading time was 10 s per cycle, followed by a 5 s hold at the maximum load and an unloading time of 10 s per each cycle. The loading was chosen so that the indentation depths ranged from approximately 50 nm to 1 μm. In total, 25 indentations were performed on each sample, with each indentation corresponding to the given depth range of 20 cycles. The load depth of the penetration data record was evaluated according to the ISO 14577 standard using the Oliver-Pharr method [59] to determine the elastic modulus E and hardness H .

Internal structure analysis by TEM

The internal structural morphology of the tested samples after Au-ion irradiation was investigated using transmission electron microscopy (TEM) and scanning transmission electron microscopy (STEM) to characterise nanoscale microstructural evolution in the sub-surface layers. STEM-HAADF (STEM-high-angle annular dark-field imaging) images were acquired with camera lengths 87 mm. Samples for TEM and STEM studies were prepared as lamellas by the focused ion beam-SEM technique using an FEI Quanta 3D electron microscope. The TEM and STEM observations were performed using an FEI Tecnai F20 field emission gun transmission electron microscope operated at 200 kV.

Results

SRIM simulations

Based on the presented SRIM calculations in section 2.1, nuclear energy stopping is the prevailing ion-stopping mechanism above 10 keV. nm⁻¹ for Au-5 MeV ion irradiation. The Cu-3 MeV ions exhibited less nuclear stopping and prevailing ionization stopping, as anticipated for lighter ions. Additionally, in HEA-Nb, we observe dpa scaling for Au-5 MeV ions in a ~ 600 nm-thick layer from 2 to 66 dpa (dpa value at maximum) at Au-ion fluences of 4×10^{14} – 1.3×10^{16} cm⁻². The Cu-5 MeV ions create at most ~ 13 dpa at depths exceeding 1 μm, as shown in Fig. 1d. We can compare also HEA-Nb with HEA-Co, HEA-Co + Y₂O₃ and Eurofer 97 as these materials were irradiated using Au-3 MeV ions with a fluence of 1.0×10^{16} cm⁻² and a maximum achievable dpa of around 50. The modified layer thickness is estimated to be about 350 nm, 600 nm and 1.5 μm for Au-3 MeV, Au-5 MeV and Cu-3 MeV ions, respectively; however, this calculation does not consider any defect migration specific to a given microstructure or gradual dynamic radiation damage.

PAS analysis of radiation defect accumulation and RBS elemental depth profiling

In the PAS analysis of defect distribution across the sample thickness, two parameters were extracted as a function of the positron energy E_p as a function of depth: S (positron annihilation with low electron momentum fraction; valence electrons) scales with the fraction of positrons trapped in open-volume defects, and W (positron annihilation with high electron momentum fraction; core electrons) indicates defects

surrounding the atom. When positrons are trapped at vacancy defects, the probability of their annihilation with valence electrons increases, while the probability of annihilation with core electrons decreases. This leads to increasing S values and decreasing W values, which are also affected by the chemical environment at the site of positron annihilation. $S(E_p)$ curves are presented for HEA-Nb irradiated with Au-5 MeV and Cu-5 MeV ions at various ion fluences in Fig. 2a and HEA-Co, HEA-Co + Y_2O_3 and Eurofer97 irradiated with Au-3 MeV at a fluence of $1 \times 10^{16} \text{ cm}^{-2}$ in Fig. 2b, c and d, respectively.

We observed an increase in defect density (demonstrated by increased $S(z_{mean})$ with depth z_{mean} in the E_p range 5–35 keV) after irradiation of HEA-Nb with Au-5 MeV ions, as shown in Fig. 2a; however, only a small correlation with ion fluence was observed. The defect concentration increases in the case of the two lowest fluences, with a slight drop recorded for the two highest fluences. In general, due to the high dpa, a positron saturation trapping regime is expected that restricts the positron-defect interactions to the suitable defect types [44]. The defect concentration does not exhibit strong depth dependence in the depth range expected for Au-5 MeV ions. After Au-ion irradiation in HEA-Nb, the damage is dispersed in the layer centred around the

theoretically predicted depth (shown by $R_p \pm \Delta R_p$ range in Fig. 2), with a broad damage distribution towards the surface and at depth.

The specific response to radiation defect accumulation in HEA based on WCrTi has recently been investigated experimentally [60] and theoretically [61], showing a defect layer broader than theoretically calculated by SRIM, with the creation of isolated dislocation far beyond the layer containing implanted Au-ions in the first mentioned one [60] and molecular dynamic simulation showing scenarios of defect dissociation and recombination in HEAs in [61].

VEPALS measurements from depths of ~ 158 – 230 nm reveal positron lifetimes of $\tau = 177 \pm 7$ ps and 169 ± 5 ps for the pristine sample and irradiated HEA-Nb samples, respectively. Given the flatness of the $S(E_p)$ trends, similar lifetimes are expected for larger depths. For Fe and the other similar elements within HEA-Nb, the lifetime range of 175–190 ps corresponds to monovacancies [62], whereas lower lifetimes are related to dislocations [63]. Vacancy-dislocation associated complexes with lifetimes slightly lower than those for monovacancies is also possible [64]. The existing literature indicates our experimental findings correspond to single vacancies [65]. For the pristine sample, a reduced lifetime is identified, validating a much lower defect

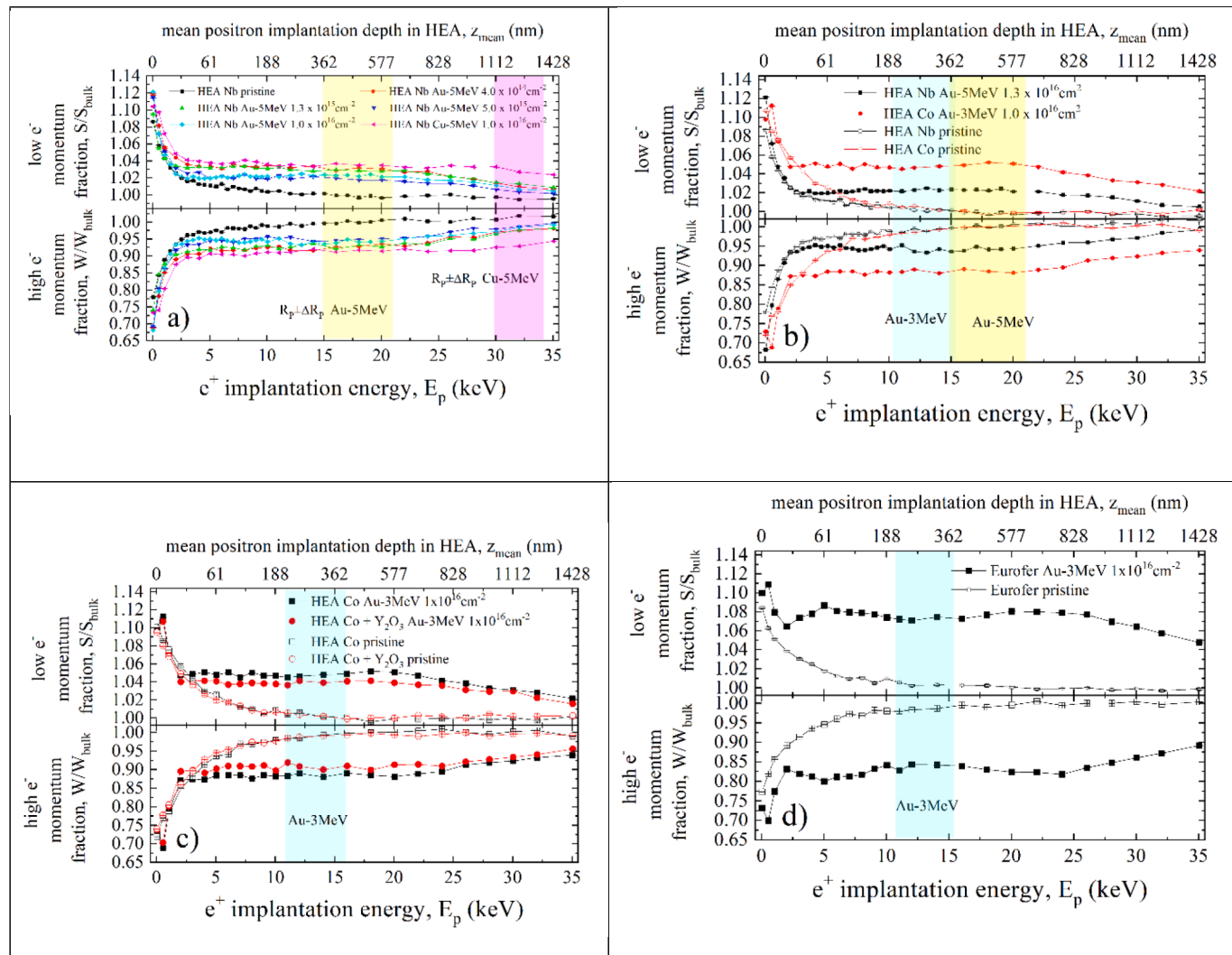


Fig. 2. DB-VEPALS positron lifetime measured S and W parameters as a function of the implanted positron energy E_p and equivalent mean depth z_{mean} in nm for a) pristine HEA-Nb and HEA-Nb irradiated with various fluences ($4 \times 10^{14} \text{ cm}^{-2}$ – $1.3 \times 10^{16} \text{ cm}^{-2}$ with Au-5 MeV and Cu-5 MeV ions). b) Comparison between HEA-Co implanted at $1 \times 10^{16} \text{ cm}^{-2}$ with Au-3 MeV ions and pristine and irradiated HEA-Nb samples with an Au-5 MeV fluence of $1.3 \times 10^{16} \text{ cm}^{-2}$. S and W parameters for c) HEA-Co and HEA-Co + Y_2O_3 samples implanted with $1 \times 10^{16} \text{ cm}^{-2}$ fluence of Au-3 MeV ions and d) pristine Eurofer97 and samples irradiated with $1 \times 10^{16} \text{ cm}^{-2}$ fluence of Au-3 MeV ions. $R_p \pm \Delta R_p$ ranges summarized in Table 2 are presented as the highlighted colour vertical bands in yellow, purple and light blue for Au-5 MeV, Cu-5 MeV and Au-3 MeV, respectively. The S and W data are normalized to the bulk value of the corresponding pristine samples.

concentration in the pre-irradiation state and classifying the observed defect lifetime of $\tau = 177 \pm 7$ ps as a major defect type in the system. Reduced lifetimes are not observed in the implanted samples, and the relative intensity of the defect lifetime is close to 100%, thus indicating positron saturation trapping after irradiation. Accordingly, it is not possible to judge the defect concentration from PALS, whereas DB-VEPAS is still sensitive to relative changes in this parameter.

The results for the Cu-5 MeV ion irradiation in HEA-Nb indicate a slightly greater defect extent in the layer from the surface to the theoretically predicted ion projection depth range (magenta curve in Fig. 2a). Even though Cu-5 MeV ions produce less dpa in the implanted layer relative to Au-5 MeV ions at the same ion fluence, the defect density is similarly high in both cases.

The comparison of HEA-Co and HEA-Nb in Fig. 2b indicates that for comparable Au-ion fluences, higher defect concentrations were identified by PAS in HEA-Co distributed within the broad layer both within and beyond the projected range of ions. This observation relates to the internal morphology and structure of HEA-Co. The grain size, number of grain boundaries and their orientation in fine-grain fusion materials (e.g. tungsten) have been shown to cause different defect sink efficiencies and grain boundaries can improve radiation tolerance due to defect annihilation [66]. Additionally, the chemical effect described in [67] can influence the migration energies of vacancies and interstitials in various XC_xFeMnNi alloys.

VEPALS measurements from depths of ~ 158 – 230 nm reveal positron lifetimes of $\tau = 225 \pm 7$ ps and 195 ± 1 ps for the HEA-Co pristine sample and irradiated sample, respectively. Hence, the pristine HEA-Co sample contains vacancy complexes close to the size of a triple-vacancy that are reduced to the size of a bi- and single-vacancy mixture [64]. The size and density of both the pristine and implanted HEA-Co defects are therefore larger than those of HEA-Nb. Additionally, because of the lattice distortion effect and higher defect concentrations in pristine HEA-Co, the ion-induced cascade would propagate not only in the initial PKA direction but in various directions in the medium. This effect would contribute to generating many defects in various directions, resulting in an overall increase in the number of defects.

We present a comparison of HEA-Co and HEA-Co + Y₂O₃ (ODS HEA) in Fig. 2c. We observed a similarity in S and W parameters' depth distribution in both HEA-Co and HEA-Co + Y₂O₃; however after Au-3 MeV irradiation with the same fluence of around 1.0×10^{16} cm⁻², the HEA-Co + Y₂O₃ exhibits a slightly lower defect concentration (i.e. lower S value). In the pristine samples, the VEPALS results indicate the same positron lifetimes, but the defect lifetime for the implanted HEA-Co + Y₂O₃ sample is slightly larger ($\tau = 198 \pm 1$ ps). The longer lifetime suggests the presence of more bi-vacancies in the system. Since the relative intensity is saturated due to the high overall damage level, it was not possible to assess the exact defect density.

A comparison of the above HEAs with PAS-analysed Eurofer97 samples presented in Fig. 2d indicates that all the HEAs exhibited better radiation resilience than Eurofer97. This pattern is very similar to the defect accumulation identified in W-based alloys in [60]. The VEPALS analysis revealed lifetimes of around $\tau = 158 \pm 3$ ps and 187 ± 3 ps for the pristine and irradiated Eurofer 97 samples, respectively. The initial defect microstructure likely comprises abundant dislocations that result in a strongly mono-vacancy-dominated crystal. In addition, a second defect lifetime component is generated ($\tau_2 = 300 \pm 15$ ps, I₂ = 22 ± 3 %), which corresponds to the range of a vacancy cluster consisting of about six vacancies [64].

RBS analysis is an elemental analytical method used for Au-depth distribution measurement that was realized here to determine the Au-depth concentration profile after the irradiation process. The Au-depth profiles were measured for the samples irradiated with the Au-3 MeV ions; these have smaller projected ranges and thus avoid the signal overlap of back-scattered projectile ions in RBS analysis. For the Au-5 MeV ions, the projected ranges are deeper below the surface, thus the Au signal overlaps with the matrix heavy element signals in the RBS spectra.

Accordingly, both Au-depth profiles for 5 MeV ion energy irradiation and Cu-depth profiles for 5 MeV ion energy were not detectable by RBS. The selected RBS-determined Au-depth profiles in HEA-Co, HEA-Co + Y₂O₃ and Eurofer97 are presented in Fig. 3, which shows excellent agreement with the Au-depth profiles simulated by SRIM presented in Fig. 1. The RBS-analysed Au-depth profiles exhibited a slight shift towards greater depth in the Au-concentration maxima and broader distributions than predicted by SRIM, which likely relates to the greater extent of penetrating ion straggling in complex-grained alloys.

Thermal effusivity and optical analysis

The scattering mean free paths of heat carriers (e.g. electrons) are sensitive to crystalline imperfections (impurities, dislocations, vacancy clusters, grain boundaries, etc.) [68]. In Fig. 4a, the thermal effusivity evolution trends over time are plotted, effectively showing the effusivity evolution with depth for the HEA-Nb samples. The analytical model described in [53,69] was applied, and the corresponding fitted thermal effusivity curves are shown in Fig. 4, where two- or three-layered systems were assumed for the fitting. The last layer represents non-affected material.

We observed a decrease in thermal effusivity (i.e. worsening of thermal properties) in the Au-5 MeV-implanted HEA-Nb compared to the pristine sample, with fluctuations in the thermal effusivity observed that did not correlate with increasing ion fluence (see Fig. 4a and Table 3). The thermal effusivity ranged from 4400 to 4700 Jm⁻².s^{-1/2}.K⁻¹ in the first layer and 2900 to 4300 Jm⁻².s^{-1/2}.K⁻¹ in the second layer compared to a value of 5100 Jm⁻².s^{-1/2}.K⁻¹ for the pristine HEA-Nb material. The thermal conductivity ranged from 2.4 to 6.3 W/m.K for irradiated samples compared to 7.2 W/m.K for the pristine material. Additionally, we observed the most significant decrease in thermal effusivity in the HEA-Nb sample irradiated with Cu-5 MeV ions. Here, the thermal effusivity decreased to 1700 Jm⁻².s^{-1/2}.K⁻¹ and the thermal conductivity decreased to 0.85 W/m.K.

The thermal effusivity of the Au-3 MeV-irradiated HEA-Co was found to be lower than that of the irradiated HEA-Nb + Y₂O₃ sample (see Fig. 4b and Table 3). This difference primarily relates to the deeper second layer in which the thermal effusivity values were found to be around 2800 and 5500 Jm⁻².s^{-1/2}.K⁻¹ and thermal conductivity 2.3 and 9 W/m.K for irradiated HEA-Co and irradiated HEA-Co + Y₂O₃, respectively.

The Eurofer97 sample exhibited a slight decrease in thermal effusivity after irradiation with Au-3 MeV at an ion fluence of 1×10^{16} cm⁻² from around 8700 to about 7900 Jm⁻².s^{-1/2}.K⁻¹ (see Fig. 4c). The thermal conductivity decreased from 20 to around 17 W/m.K after the irradiation, with this change observed over only a small depth range of about 200 nm. A summary of the measured thermal effusivities in various layers in the irradiated HEAs is presented in Table 3.

Optical properties of samples

The measured optical properties of Eurofer and HEA-Co pristine vs those of the irradiated samples are shown in Fig. 5a. The same ion fluence of 1×10^{16} ions.cm⁻² and ion beam energy (Au-3 MeV) were used. In the case of the HEA-Co samples and Eurofer, the irradiated samples show lower reflectivity values than the pristine samples, especially at shorter wavelengths. These differences relate to changes in the samples' surface morphology before and after irradiation, either due to roughness increases [56] or decreases in electron mobility (by reducing electrical conductivity). Novakowski et al. [30] found that ion bombardment modifies the surface morphology of materials, e.g. in response to He ion irradiation at fluences up to 10^{24} – 10^{25} ions.cm⁻². The ion fluences used in our present study are several orders of magnitude lower but much heavier Au-ions were used; thus the surface morphology modifications are interpreted as a likely cause of the observed decreases in reflectivity.

A comparison between HEA-Co, HEA-Nb and Eurofer irradiated samples is shown in Fig. 5b. HEA-Nb with lower ion fluence (1.3×10^{15}

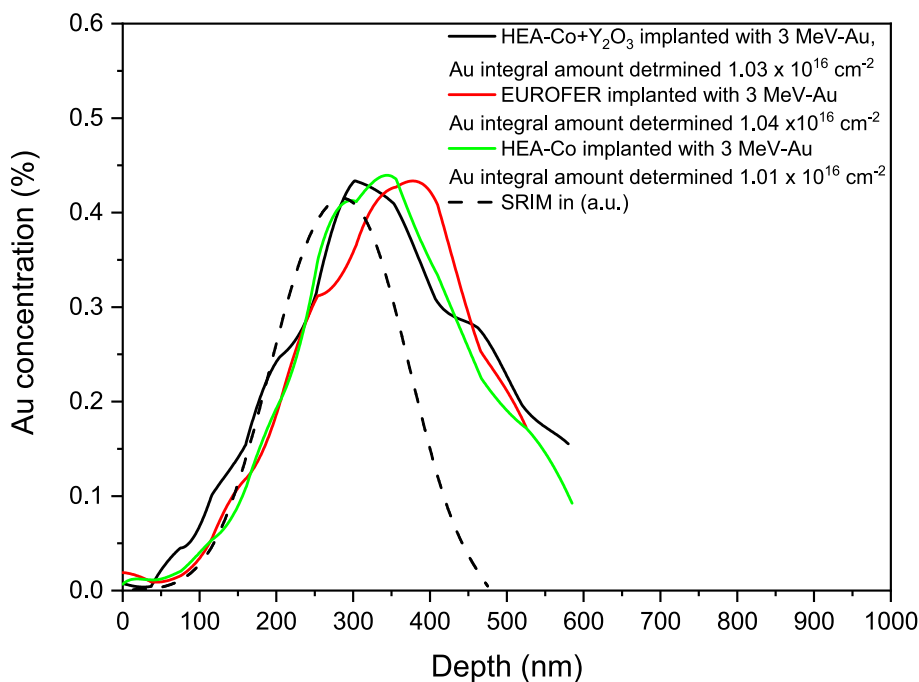


Fig. 3. RBS analysis of the implanted Au-depth profiles for Co-HEA, Co-HEA + Y_2O_3 and Eurofer97 samples implanted with Au-3 MeV ions and the same ion fluence (nominally $1.0 \times 10^{16} \text{ cm}^{-2}$).

ions cm^{-2}) has significantly higher reflectivity than the HEA-Nb sample irradiated with an ion fluence of $1.3 \times 10^{16} \text{ ions cm}^{-2}$, especially at wavelengths below $0.9 \mu\text{m}$. In contrast, Eurofer irradiated with lower Au-ion energy (3 MeV) and HEA-Nb irradiated with higher Au-ion energy (5 MeV) show similar reflectivity values for the $0.3\text{--}0.9 \mu\text{m}$ wavelength range; however, notable differences are observed in the near-infrared wavelength region. This variance may be caused by the elemental composition of samples and different ion-implantation parameters. Broadly, the reflectivity increases with increasing wavelength.

X-ray diffraction

The XRD results from this study are summarized in Table 4. HEA-Co is a single-phase face-centred cubic (fcc) material. In both its variants (homogeneous and with ODS), a moderate decrease in crystalline size and a moderate increase in microstrain were observed after Au-ion 3 MeV irradiation. In Eurofer, the relative change in crystalline size after the irradiation was comparable to that of HEA-Co; however, a greater increase in microstrain was observed, indicating more intense lattice defect formation, as previously identified from the PAS results. These findings suggest greater irradiation resilience of HEA-Co compared to Eurofer steel.

HEA-Nb is a complex multi-phase material in which three major phases were distinguished and used for the analysis. A detailed analysis of the phase composition is beyond the scope of this paper; thus, phases with a similar structure were used in the Rietveld refinement, namely fcc Ni (space group Fm-3 m) denoted as phase 1, MnO (Fm-3 m) denoted as phase 2 and Fe₂W (P63/mmc) denoted as phase 3 in Table 4. The microstructural parameters were evaluated only for the dominant phase, i.e. fcc-Ni-like phase 1. The changes in microstructural parameters due to irradiation are considered insignificant. However, an evolution in phase composition was observed; while the content values of phases 1 and 2 remained similar, the phase 3 content decreased in the samples irradiated by Au and Cu ions. Presence of an amorphous ‘hump’ in the irradiated HEA-Nb diffractograms was observed for the irradiated samples (Fig. S3) Due to the complex nature of the HEA-Nb material and the possible presence of texture in the samples, the phase analysis results should be taken as semi-quantitative only.

Mechanical properties – nano-indentation

The nanoindentation measurement results are presented in Fig. 6, where hardness H is shown as a function of depth. At small contact depths, a significant indentation size effect (ISE), i.e. increase in hardness with decreasing indentation depth, was observed for all unirradiated and irradiated samples.

At shallow depths, the irradiated samples all have demonstrably higher hardness than non-irradiated samples, except for HEA-Nb, in which the irradiation had practically no effect. The lack of irradiation effect on the hardness in HEA-Nb (where the Au-ion irradiation does not cause any further hardness increase) likely relates to the inherent hardness of the HEA-Nb, i.e. the material cannot harden further (see Fig. 6a). In HEA-Co, more significant hardness enhancement is observed in the surface layer to a depth of 500 nm based on the penetration of Au ions with 3 MeV energy (see Fig. 6b). In contrast, Eurofer97, being the softest of the tested materials, exhibited the most pronounced change in hardness following irradiation (see Fig. 6c). Due to the low irradiated layer thickness, the values are probably influenced by a ‘softer’ (unirradiated) substrate almost from the beginning of the measurements for all the irradiated samples; accordingly, it was not possible to separate the ISE and irradiation effects or extrapolate the effect of irradiation on changes in the samples’ macroscopic mechanical properties.

The modulus of elasticity E remained approximately constant for all samples over the whole range of measured depths, with no effect observed in response to irradiation (as expected). The E values were, however, slightly overestimated (e.g. 230 GPa for Eurofer instead of the expected approximately 200 GPa) indicating possible underestimation of the contact area due to the occurrence of pile-up, which was confirmed by the confocal microscopy. The observed pile-up was greater in the unirradiated samples than in the irradiated samples; however, this effect is more likely due to the presence of a harder layer on the softer substrate rather than the irradiated material itself having a lower tendency to form a pile-up.

TEM

TEM analysis was performed to gain insights into the material

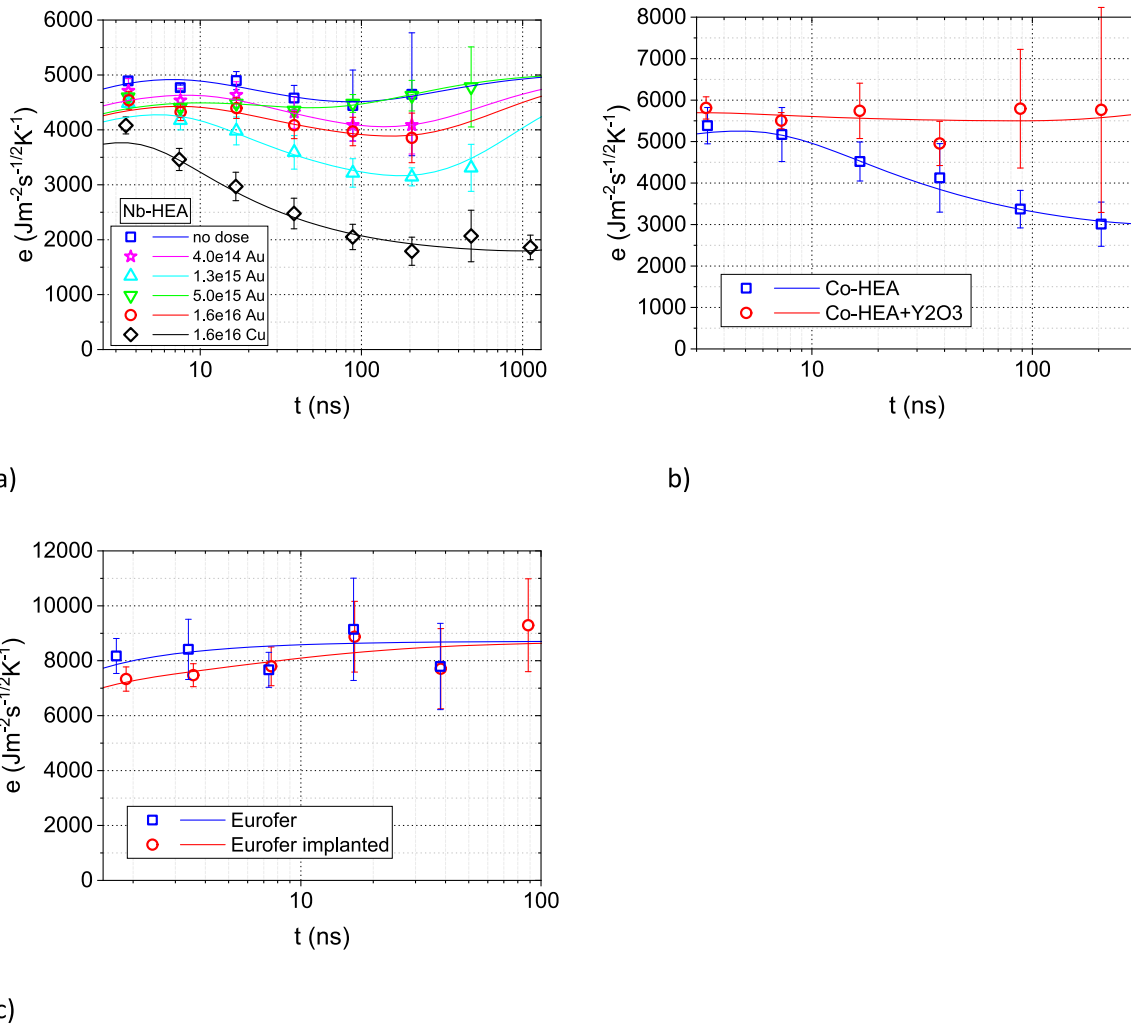


Fig. 4. Thermal effusivity as a function of time of a) pristine HEA-Nb (NbCrFeMnNi) and Au-5 MeV and Cu-5 MeV ion-irradiated HEA-Nb samples, b) HEA-Co (CoFeCrMnNi) and HEA-Co + Y₂O₃ and c) Eurofer97. The fitted curves for the various layer thicknesses and thermal conductivities in the layers are also shown. Details of the fitted thermal effusivities for various depths are described in the main text.

Table 3

Thermal properties and thickness of the surface and subsurface layers for HEA samples after Au-5 MeV, Cu-5 MeV and Au-3 MeV ion irradiation as determined by thermal effusivity measurements and model fitting.

Sample /ion type	Irradiation fluence (cm^{-2})	Thermal effusivity ($\text{Jm}^{-2}\text{s}^{-1/2}\text{K}^{-1}$)		Thermal conductivity ($\text{W.m}^{-1}\text{K}^{-1}$)		Layer thickness (nm)	
		First layer	Second layer	First	Second	First	Second
HEA-Nb Au-5 MeV	4.0×10^{14}	4742	3825	6.3	4.1	230	500
HEA-Nb Au-5 MeV	1.3×10^{15}	4431	2927	5.5	2.4	180	500
HEA-Nb Au-5 MeV	5.0×10^{15}	4589	4266	5.9	5.1	200	300
HEA-Nb Au-5 MeV	1.3×10^{16}	4550	3731	5.8	3.9	200	600
HEA-Nb Cu-5 MeV	1.0×10^{16}	4008	1742	4.5	0.85	125	1000
HEA-Nb	—	5069	4308	7.2	5.2	200	400
HEA-Co Au-3 MeV	1.0×10^{16}	5477	2769	9	2.3	230	800
HEA-Co + Y ₂ O ₃ Au-3 MeV	1.0×10^{16}	6324	5477	12	9	100	1000
Eurofer pristine	—	8714	—	—	20	—	—
Eurofer Au-3 MeV	1.0×10^{16}	—	7915	—	16.5	—	200

microstructure and observe the types of radiation damage. The HEA-Co alloys exhibited a rough grain structure (Fig. 7), with grains of $\sim 200\text{--}500$ nm size. TEM analysis of the pristine HEA-Co (Fig. 7a) and HEA-Co after irradiation (Fig. 7b) indicate the presence of a defect-bearing sub-surface layer with a maximum defect concentration at a depth of 700 nm. The black precipitates were identified as MnCr₂O₄ by EDX as a probable product of sintering. The TEM analysis identified

defects deeper than the predicted Au-3 MeV ion ranges in Fig. 1c based on SRIM simulations. A very similar depth distribution of defects was identified in the HEA-Co + Y₂O₃ samples (Fig. 7c and 7d). However, the bright spots attributed to implanted Au clusters in the layer (see Fig. 7d).

In the case of HEA-Nb irradiated with Au-5 MeV ions with a fluence of $1.3 \times 10^{15} \text{ cm}^{-2}$, s shown in Fig. 8a. HEA-Nb exhibited finer grain structure compared to HEA-Co (see Fig. 7b and Fig. 8b, respectively).

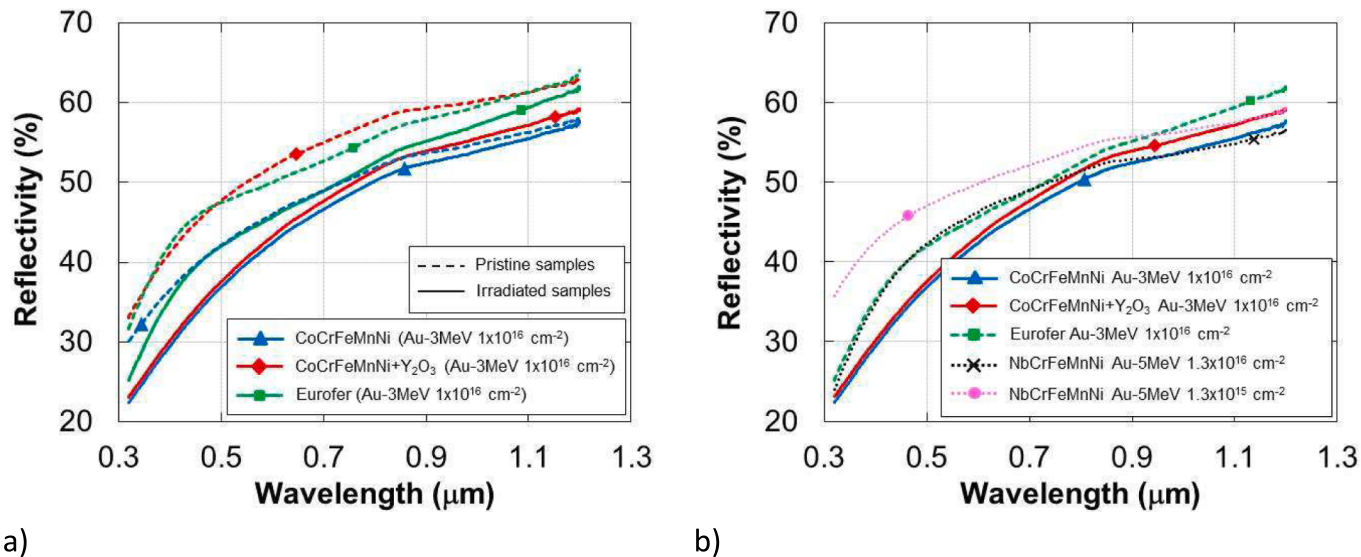


Fig. 5. a) Spectral normal hemispherical reflectivity comparison of pristine and irradiated (Au-3 MeV ions at ion fluence of $1 \times 10^{16} \text{ cm}^{-2}$) HEA-Co, HEA-Co + Y_2O_3 and Eurofer samples in the wavelength range 0.3–1.2 μm , and b) diffuse spectral normal hemispherical reflectivity of HEA-Co, HEA-Co + Y_2O_3 and Eurofer97 samples irradiated with Au-3 MeV ions at an ion fluence of $1 \times 10^{16} \text{ cm}^{-2}$ and of HEA-Nb samples irradiated with Au-5 MeV at various ion fluences in the wavelength range 0.3–1.2 μm .

Table 4

Summary of the XRD results. Crystallite size refers to the size of coherently diffracting domains (CDDs), while the ‘ratio’ represents the ratio of a given variable in the irradiated sample vs. that in the corresponding pristine sample. The penetration of X-rays is higher than the depth of the irradiated layer, thus the results are somehow averaged from irradiated and unirradiated volume.

	Crystallite size	Ratio	Microstrain	Ratio	Phase 1	Phase 2	Phase 3
	nm				wt%	wt%	wt%
HEA-Co pristine	182		0.00045				
HEA-Co Au-irradiated	164	0.90	0.00051	1.13			
HEA-Co + Y_2O_3 pristine	180		0.00041				
HEA-Co + Y_2O_3 Au-irradiated	155	0.86	0.00049	1.20			
Eurofer97 pristine	190		0.00018				
Eurofer97 Au-irradiated	174	0.92	0.00028	1.56			
HEA-Nb pristine	113		0.00067		50	25	26
HEA-Nb Au-irradiated	131	1.16	0.00069	1.03	57	28	15
HEA-Nb Cu-irradiated	130	1.15	0.00069	1.03	65	23	12

Individual grains in the samples were identified based on their elemental composition. Points 2–4 and 6 in Fig. 8c were characterized by high Nb content and amorphisation following irradiation with an Au ion fluence of $1.3 \times 10^{15} \text{ cm}^{-2}$. Points 1, 5 and 8 do not contain Nb, and the black grains at these locations contain oxides. These grains did not exhibit significant changes in response to Au ion irradiation. The other images of the HEA-Nb samples (irradiated with Au-5 MeV ions with a fluence of $4 \times 10^{14} \text{ cm}^{-2}$ in Fig. 8b and Au-5 MeV-Au ions with a fluence of $1.3 \times 10^{15} \text{ cm}^{-2}$ in Fig. 8a) reveal similar trends, with amorphisation recorded in the upper 1 μm layer proved by selected area electron diffraction (SAED) shown as inset in Fig. 8b, without significant correlation with the ion fluence. These findings are consistent with the PAS findings and reveal comparable defect sizes and concentrations for the studied ion fluences.

Discussion

In this study, HEA-Nb, HEA-Co and HEA-Co + Y_2O_3 complex high-entropy alloys were investigated from the perspective of radiation defect introduction under ion irradiation and compared to conventional Eurofer97 material. The following effects were investigated: (i) radiation defect concentration and sizes and their depth distribution for various Au-ion fluences and a comparison of Au- and Cu-ion bombardments at the same ion energies and fluences in terms of collision cascade

density and extent of collision effects, (ii) the effect of defect accumulation in various HEA-constellations/compositions and (iii) the effect of defect formation in terms of mechanical and thermal properties.

The theoretical SRIM calculations predict that Au-5 MeV ion irradiation should have a lower penetration depth of about half a micron, with energy deposition predominantly via ballistic collisions (around twice that of ionisation processes), corresponding to the highly likely formation of Frenkel pairs and vacancies. In contrast, the Cu-5 MeV ions were predicted to have a penetration depth exceeding 1 μm with energy primarily via ionisation; in this instance, energy loss via ballistic processes was predicted to be half that of ionisation. The maximum dpa created by Cu-5 MeV ions was predicted to be around five times lower than that of Au-5 MeV ions at a comparable ion irradiation fluence. Theoretical SRIM simulations were performed to assess predicted energy stopping, dpa depth profile calculation through nuclear stopping and the projected ranges of the studied Au and Cu ions. The depth distribution of Au ions was detected by RBS for the implanted Au-3 MeV samples. In the case of these samples, the RBS analysis was able to determine the Au-depth profiles due to the shallower implantation depth; however, in the case of Au-5 MeV, very similar results would be expected consistent with SRIM predictions. Thus, Au specie distribution is very well-localised and consistent with theoretical predictions; however, the defect depth development determined by PAS exhibited high complexity and a much broader depth distribution.

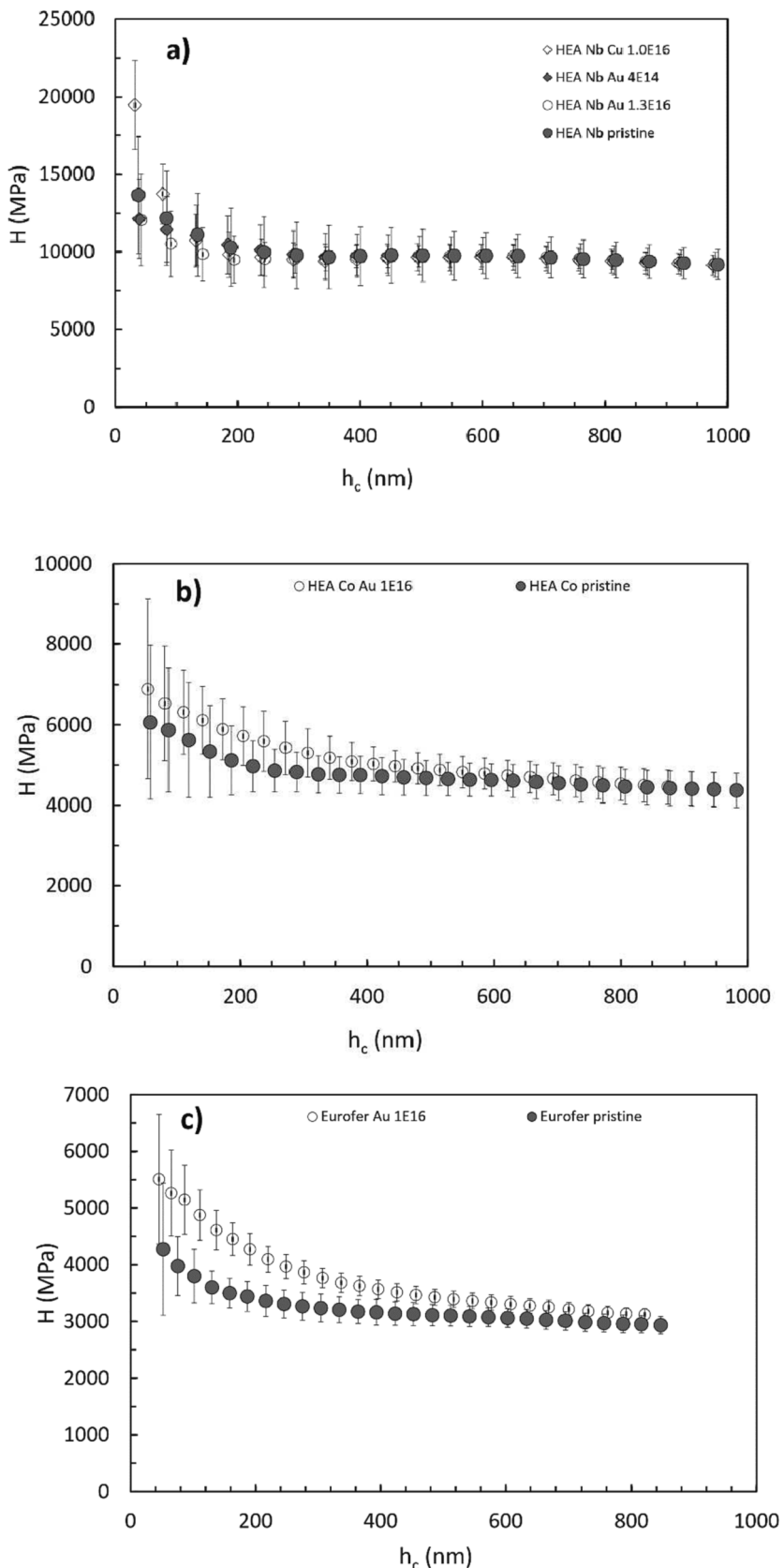


Fig. 6. Hardness measured by the nanoindentation method for a) HEA-Nb irradiated with the 5 MeV-Au ions at the lowest and the highest fluences and 5 MeV-Cu ions with a fluence of $1.0 \times 10^{16} \text{ cm}^{-2}$, b) HEA-Co and d) HEA-Co with dispersed Y_2O_3 irradiated with 3 MeV-Au ions with an ion fluence of $1.0 \times 10^{16} \text{ cm}^{-2}$, and c) EUROFER irradiated with the 3 MeV-Au ions with an ion fluence of $1.0 \times 10^{16} \text{ cm}^{-2}$.

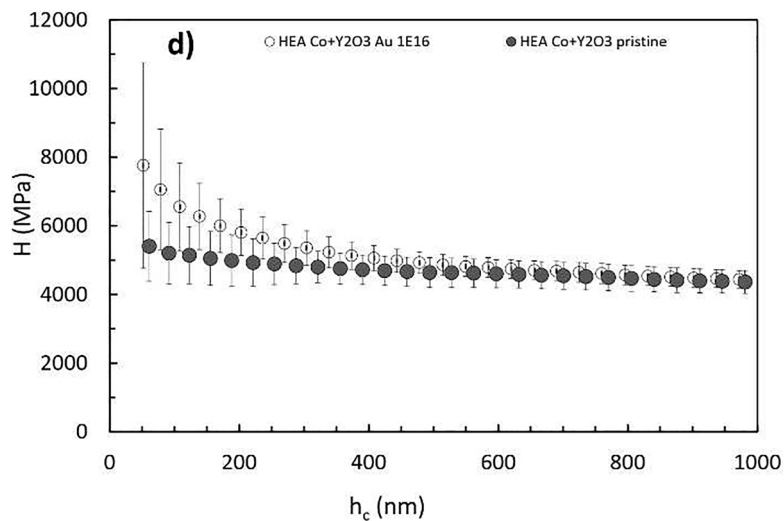


Fig. 6. (continued).

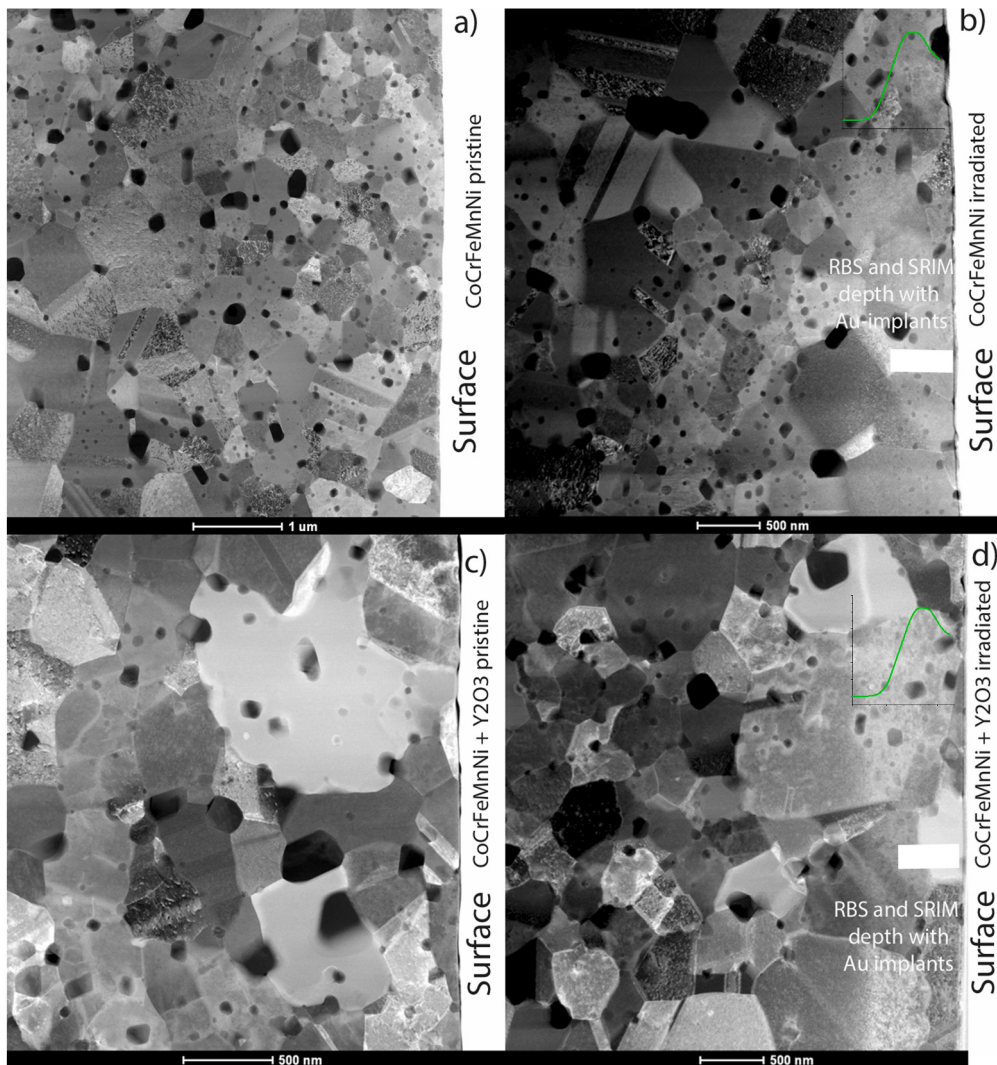


Fig. 7. STEM analysis of interior morphology of a) HEA-Co pristine and b) HEA-Co irradiated with Au-3 MeV ions with an ion fluence of $1.0 \times 10^{16} \text{ cm}^{-2}$. STEM analysis of c) HEA-Co + Y_2O_3 pristine and d) HEA-Co + Y_2O_3 irradiated with Au-3 MeV ions with an ion fluence of $1.0 \times 10^{16} \text{ cm}^{-2}$. The corresponding dpa depth profiles calculated by SRIM are shown as green curves in insets in b) and d), where on x-axis is depth in nm appropriate to the scale used in STEM.

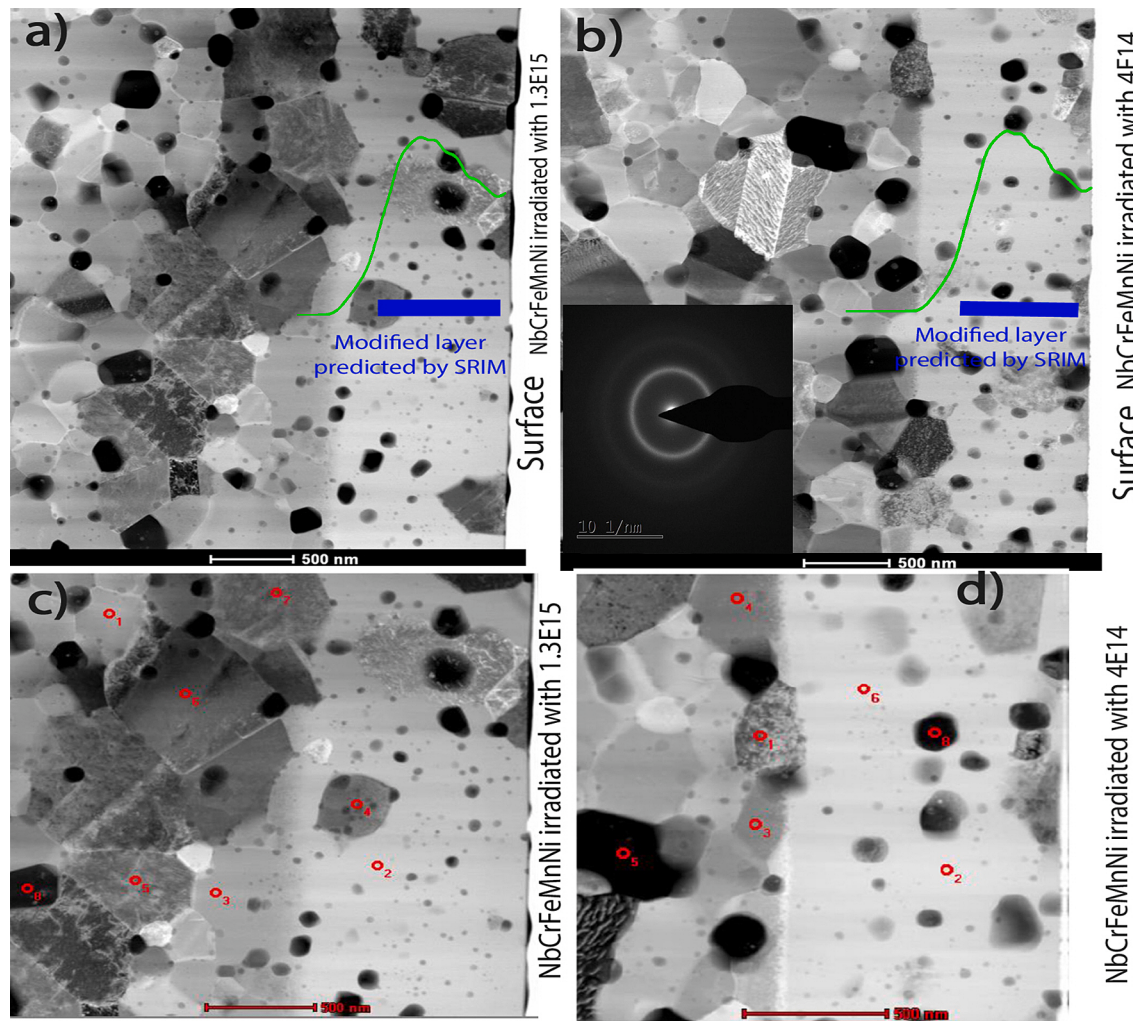


Fig. 8. STEM analysis of the interior morphology of HEA-Nb samples (NbCrFeMnNi) irradiated with Au-5 MeV ions with ion fluences of a) $1.3 \times 10^{15} \text{ cm}^{-2}$ and b) $4 \times 10^{14} \text{ cm}^{-2}$. STEM-EDX elemental analysis is also shown for the HEA-Nb samples irradiated with Au-5 MeV ions at ion fluences of c) $1.3 \times 10^{15} \text{ cm}^{-2}$ and d) $4 \times 10^{14} \text{ cm}^{-2}$. The sample points (grains) denoted 2, 3, 4 and 6 in c) have high Nb contents of around 28 at. %, whereas points 1,5 and 8 have negligible or no Nb content. Points 1, 2 and 3 in d) have high Nb contents of around 30 at. %, while points 4–8 have negligible or no Nb content. The corresponding dpa depth profiles calculated by SRIM are shown as green curves in insets in a) and b), where on x-axis is depth in nm appropriate to the scale used in STEM. Inset in b) shows selected area electron diffraction (SAED) from the irradiated part.

The defect concentration and sizes were investigated by PAS, revealing a broad damaged layer with defect accumulation beyond the projected ranges of Au-5 MeV (461 nm), Au-3 MeV (284 nm) and Cu-5 MeV (1311 nm) ions calculated by SRIM. The PAS analysis identified a broad layer with defects from the surface to a depth of $\sim 1 \mu\text{m}$ without a significant maximum in all Au and Cu ion-implanted samples. The PAS measurements in HEA-Nb indicate mainly single monovacancies and defect concentration saturation at low Au-ion fluences; however, PAS cannot be used to accurately determine the defect concentration due to the highly defective structure of the samples.

Similar effect of defect dissipation beyond the predicted range of ions has previously been observed in W-based HEAs in [60] and it has been ascribed to easier defect migration within the irradiated layer. The theoretical background for specific HEA-radiation tolerance and defect fragmentation rather than accumulation was recently presented in [61], where defects moved primarily as individual single defects rather than clusters during defect evolution. This behaviour contrasts with the reported defect evolution in pure metals, where defect movement was reported in the form of interstitial clusters containing dislocations.

The configurational and compositional complexities in HEAs are thought to not only slow energy dissipation pathways [70], but also to cause site-to-site lattice distortion [27] that can complicate the energy

landscape for defect migration. These effects may both synergically alter defect dissipation/migration and can influence the radiation tolerance of HEAs with different elemental compositions.

HEA-Nb exhibited the least damage accumulation among the studied alloys with no strong relation to the Au-5 MeV ion implantation fluence, in contrast to the enhancement of defect concentration and sizes identified by PAS in the Au ion-implanted Eurofer97 and HEA-Co samples. HEA-Co contains a higher concentration of pre-existing defects in pristine samples which may be connected to the lattice distortion. HEA-Co contains vacancy complexes close to the size of a triple-vacancy that are reduced to the size of a bi- and single-vacancy mixture after the irradiation. The addition of yttrium oxide into HEA-Co + Y₂O₃ does not lead to a significant decrease in defect concentration or size after irradiation compared to HEA-Co.

The HEA-Co + Y₂O₃ sample does not show significantly lower defect concentration after irradiation compared to HEA-Co; however, significant differences in internal morphology and mechanical properties were identified in our previous study [38], including a 50% grain size reduction compared to HEA-Co, ultimate tensile strength and yield strength enhancements of 30% at room temperature.

More effective defect recombination in HEA-Nb can be linked also to the microstructure of HEA-Nb, which exhibits smaller grain sizes with

finer microstructure compared to HEA-Co, as observed in the TEM analysis. This phenomenon has also previously been reported in the literature [67].

Eurofer97 was expected to exhibit the highest defect concentration enhancement and defect sizes in comparison with HEAs, which was confirmed by the PAS analysis results, where six-vacancy clusters were identified with high probability. HEA-Co both with and without dispersed Y_2O_3 revealed less damage accumulation than Eurofer97 but more than occurred in HEA-Nb. The specifics of the HEA local chemistry produce migration energy barriers, in contrast to alloys with a predominant single element such as Eurofer97. The low energy tails of this migration energy distribution lead to more rapid recombination of Frenkel pairs relative to elementally pure lattices [61].

The complexity of HEAs can cause the formation of more localised PKAs, which gives Frenkel pairs more time to recombine and increases the radiation hardness [32]. However, we observed similar defect accumulation for HEA-Nb irradiated with Cu-5 MeV and Au-5 MeV ions using similar ion irradiation fluences, which reveals the non-negligible role of ionisation in defect creation, which can lead to more pronounced lattice distortion. Some authors have suggested [32,27] that the initial damage caused by the cascade is enhanced in HEAs by high inter-atomic stress levels resulting from the atomic size differences in HEA with varied elemental compositions. These stresses facilitate easier amorphisation of HEAs by the displacement cascade mechanism, similar to the effect of increasing temperature on amorphisation and melting (i.e. increased thermal vibrations aid melting).

The XRD analysis qualitatively shows that the coherent domain sizes after irradiation decrease with simultaneous microstrain development in Eurofer97 and HEA-Co, consistent with the findings described above. HEA-Nb does not show coherent domain size modification or microstrain evolution after the irradiation but instead exhibits a different response with various phase modifications under irradiation. Based on these findings, we suggest that HEA-Co primarily developed lattice strain and distortion, which inhibit radiation defect recombination.

The SRIM average thicknesses of the dpa depth distribution, PAS defected layer average thickness and RBS-determined Au-enriched layer thickness results are summarised in Table 5. As shown, there is a reasonable agreement in the dpa maximum localisation predicted by SRIM and measured by PAS with slight broadening towards the depth in HEA-Nb, contrary less agreement is evidenced in HEA-Co and Eurofer97. The mentioned findings described above were also confirmed by the hardness measurements and thermal property analysis, which revealed a decrease in thermal effusivity after irradiation in the sub-surface layer thickness in agreement with PAS analysis, except Eurofer97 see Table 5. The maximum hardness increase was evidenced in Eurofer97 compared to the smallest hardness increase in HEA-Nb in the shallow sub-surface layer. The thermal property deterioration occurred at depths consistent with the PAS-identified defect layer, as shown in Table 5. It has previously been suggested that the primary lower thermal conductivity associated with the complex compositions of concentrated alloys leads to reduced energy dissipation immediately following the displacement cascade; thus, lower thermal effusivity in pristine samples may indicate better resistance to irradiation [70]. The lowest thermal effusivity was observed in HEA-Nb and the highest in Eurofer97, while HEA-Co had an intermediate thermal effusivity value.

The TEM results reveal the presence of a defect-bearing layer in reasonable agreement with the dpa depth profiles, and the Au-precipitates identified by TEM agrees with the SRIM depth prediction as well. TEM confirmed rather small-size defects in the irradiated layer of HEA-Nb and HEA-Co. The TEM results revealed interesting phenomena in HEA-Nb samples, including preferential amorphization of Nb grains relative to grains without Nb content and a finer-grained structure compared to HEA-Co. Grains with low Nb content and oxide content do not exhibit significant changes after irradiation, which may relate to variations in interatomic stress, symmetry and chemical surroundings due to differences in the elemental content of grains [27]. The sintering

Table 5

Comparison of defected layer thicknesses and Au ion distribution depths (if available) for HEAs and Eurofer97 as determined by SRIM simulation and PAS and RBS analyses, in addition the modified layer thicknesses with changed thermal and mechanical properties are presented. Hardened layer was defined as the depth in an irradiated sample with a 10% increase in hardness above the pristine sample.

	SRIM Dpa average thickness of distribution (nm)	PAS Defected layer thickness (nm)	RBS Au enriched layer - average thickness (nm)	Thermal effusivity worsening – layer thickness (nm)	Hardened layer/layer thickness (nm)
HEA-Nb Au-5 Mev ions	0-600	30-850	N/A	0-800	*
HEA-Nb Cu-5 Mev ions	0-1500	30-1400	N/A	0-1100	N/A
HEA-Co Au-3 MeV ions	0-350	30-830	200-450	0-1000	<300
HEA-Co + Y_2O_3 Au-3 MeV ions	0-350	30-830	200-450	0-1000	<300
Eurofer97 Au-3 MeV ions	0-350	30-830	200-470	0-200	<500

N/A indicates that this analysis was not performed.

*no hardened layer was detected.

of the HEA-Nb has resulted in a multi-phase material, where the individual phases had different composition and our results indicate that different phases apparently react differently to the irradiation. The TEM analysis also confirmed that HEA-Nb has comparable defect accumulation at various ion fluences in a broad layer, as shown by PAS; in addition, HEA-Co samples both with and without dispersoid Y_2O_3 do not exhibit significant damage accumulation differences after irradiation, as discussed above.

Conclusion

In this study, HEAs (HEA-Co (CoCrFeMnNi), HEA-Nb (NbCrFeMnNi) and Eurofer97) were irradiated with various ion masses (Cu and Au ions) and ion energies (3 and 5 MeV) to determine dpa development, radiation defect accumulation and internal morphology. Dpa values in the range of 1-66 were achieved using Cu and Au ion fluences ranging from 4×10^{14} to $1.3 \times 10^{16} \text{ ions.cm}^{-2}$ at room temperature to generate various levels of lattice damage. Theoretical simulations were performed to predict the energy stopping and radiation damage depth using SRIM code, which were then compared to Au-depth profiles determined using RBS (Rutherford Back-Scattering spectrometry). The PAS (Positron Annihilation Spectroscopy) analysis identified the lowest defect concentration and size in HEA-Nb, corresponding mainly to single vacancies. Higher defect concentrations were identified in HEA-Co and HEA-Co + Y_2O_3 , which contained triple vacancies with some possible reduction to double vacancies. HEAs exhibited smaller defects compared to Eurofer 97, where largest defects were identified by PAS. Defects are dissipated in the broad layer beyond the projected ranges of ions in all samples supposing long-range defect migration in case of simpler defects, more effective defect recombination and multi-direction PKAs distribution in collision cascades in the complex microstructure of HEAs.

The XRD (X-ray Diffraction) results shows that the coherent domain sizes decreased in HEA-Co after irradiation, additional microstrain enhancement was also observed. Largest defect sizes has been created in Eurofer97 and smallest in HEA-Nb. HEA-Nb shows exhibits a different response with various phase modifications under irradiation. The thermal property analysis showed a decline in thermal effusivity after irradiation in all samples within a depth range consistent with the PAS-identified defected layer thickness. In addition, greater hardness enhancement was identified in Eurofer 97 and HEA-Co relative to HEA-Nb.

CRediT authorship contribution statement

A. Mackova: Investigation, Conceptualization, Funding acquisition, Writing – original draft. **V. Havránek:** Conceptualization, Methodology, Validation. **R. Mikšová:** Data Curation, Formal analysis. **S. Fernandes:** Data acquisition, Conceptualization. **J. Matejicek:** Data curation, Investigation, Writing – review & editing. **H. Hadraba:** Data curation, Investigation, Writing – review & editing. **M. Vilemová:** Data curation, Investigation, Writing – review & editing. **M.O. Liedke:** Investigation, Visualization, Data curation. **J. Martan:** Investigation, Visualization, Data curation. **M. Vronka:** Investigation, Data curation. **P. Haušild:** Investigation, Data curation, Formal analysis. **M. Butterling:** Investigation, Data curation, Formal analysis. **P. Honnerová:** Investigation, Data curation. **A.G. Attalah:** Data curation. **A. Wagner:** Data curation. **F. Lukac:** Data curation.

Declaration of Competing Interest

The authors declare that they have no known competing financial interests or personal relationships that could have appeared to influence the work reported in this paper.

Data availability

Data will be made available on request.

Acknowledgements

This research was conducted at the CANAM (Centre of Accelerators and Nuclear Analytical Methods) infrastructure LM 2015056. Preparation of the alloys was supported by the Czech Science Foundation project no. 17-23964S. This publication was supported by the project Strategy AV 21 of the Czech Academy of Sciences. The research was also supported by the Ministry of Education, Youth and Sports of the Czech Republic (LABIR-PAV project, No. CZ.02.1.01/0.0/0.0/18_069/0010018). The micromechanical characterization was also partially financed by the European Regional Development Fund in the framework of the project Centre of Advanced Applied Sciences (No.CZ.02.1.01/0.0/0.0/16_019/0000778). Parts of this research were also conducted ELBE at the Helmholtz-Zentrum Dresden-Rossendorf e. V., a member of the Helmholtz Association. We would like to thank the facility staff (Eric Hirschmann) for their assistance. This work was also partially supported by the Impulse and Networking Fund of the Helmholtz Association (FKZ VH-VI-442 Memriox) and the Helmholtz Energy Materials Characterization Platform (03ET7015). In addition, we acknowledge the Czech NanoLab Research Infrastructure supported by MEYS CR (LM2023051).

Appendix A. Supplementary data

Supplementary data to this article can be found online at <https://doi.org/10.1016/j.nme.2023.101510>.

References

- [1] R. Rayaprolua, S. Möller, R. Abernethy, M. Rasinski, J.C. Haley, C.h. Linsmeier, Indentation testing on 3 MeV proton irradiated tungsten, *Nucl. Mater. Energy* 25 (2020), 100776.
- [2] M. Abdou, N.B. Morley, S. Smolentsev, A. Ying, S. Malang, A. Rowcliffe, M. Ulrickson, Blanket/first wall challenges and required r&d on the pathway to demo, *Fusion Eng. Des.* 100 (2015) 2–43.
- [3] M.R. Chen-Hsi Huang, J.M. Gilbert, Simulating irradiation hardening in tungsten under fast neutron irradiation including reproduction by transmutation, *J. Nucl. Mater.* 499 (2018) 204–215.
- [4] B.I. Khrupunov, S. Koidan, A.I. Ryazanov, V.M. Gureev, S.N. Kornienko, S. T. Latushkin, A.S. Rupyshev, E.V. Semenov, V.S. Kulikauskas, V.V. Zatekin, Study of Tungsten as a Plasma-facing Material for a Fusion Reactor, *Phys. Procedia* 71 (2015) 63–66.
- [5] J.-W. Yeh, Recent progress in high-entropy alloys, *Ann. Chim. Sci. Matér.* 31 (2006) 633–648.
- [6] M.H. Tsai, J.W. Yeh, High-Entropy Alloys: A Critical Review, *Mater. Res. Lett.* 2 (2014) 107–123.
- [7] Y.F. Ye, Q. Wang, J. Lu, C.T. Liu, Y. Yang, High-entropy alloy: challenges and prospects, *Mater. Today* 19 (2016) 349–362.
- [8] B. Gwaliani, R.M. Pohan, J. Lee, B. Lee, R. Banerjee, Ho Jin Ryu, Soon Hyung Hong, High-entropy alloy strengthened by in situ formation of entropy stabilized nano-dispersoids, *Sci. Rep.* 8 (2018) 14085.
- [9] Z. Tang, T. Yuan, C. Tsai, J. Jeh, Fatigue behavior of a wrought Al0.5CoCrCuFeNi two-phase high-entropy alloy, *Acta Mater.* 99 (2015) 247–258.
- [10] H.R. Sistla, J.W. Newkirk, F. Liou, Effect of Al/Ni ratio, heat treatment on phase transformations and microstructure of AlxFeCoCrNi2-x ($x=0.3, 1$) high entropy alloys, *Mater. Des.* 81 (2015) 113–121.
- [11] Z. Fu, W. Chen, H. Xiao, L. Zhou, D. Zhu, S. Yang, Fabrication and properties of nanocrystalline Co0.5FeNiCrTi0.5 high entropy alloy by MA-SPS technique, *Mater. Des.* 44 (2013) 535–539.
- [12] J.Y. He, H. Wang, H.L. Huang, X.D. Xu, M.W. Chen, Y. Wu, X.J. Liu, K. An, Z.P. Lu, A precipitation-hardened high-entropy alloy with outstanding tensile properties, *Acta Mater.* 102 (2015) 187–196.
- [13] D.J.M. King, S.C. Middleburgh, A.G. McGregor, M.B. Cortie, Predicting the formation and stability of single phase high entropy alloys, *Acta Mater.* 104 (2016) 172–179.
- [14] I. Toda-Caraballo, P.E.J. Rivera-Díaz-Del-Castillo, Modelling solid solution hardening in high entropy alloys, *Acta Mater.* 85 (2014) 14–23.
- [15] N.N. Guo, L. Wang, L. Luo, X.Z. Li, Y. Su, J. Guo, H. Fu, Microstructure and mechanical properties of refractory MoNbHfZrTi high-entropy alloy, *Mater. Des.* 81 (2015) 87–94.
- [16] F. Otto, Y. Yang, H. Bei, E.P. George, Relative effects of enthalpy and entropy on the phase stability of equiatomic high-entropy alloys, *Acta Mater.* 61 (2013) 2628–2638.
- [17] F. Otto, A. Dlouhý, C.h. Somsen, H. Bei, G. Eggeler, E.P. George, The influences of temperature and microstructure on the tensile properties of a CoCrFeMnNi high-entropy alloy, *Acta Mater.* 61 (2013) 5743–5755.
- [18] B. Cantor, I.T.H. Chang, P. Knight, A.J.B. Vincent, Microstructural development in equiatomic multicomponent alloys, *Mater. Sci. Eng.: A* 375 (2004) 213–218.
- [19] N.N. Stepanov, M. Tikhonovsky, N. Yurchenko, D. Zyabkin, M. Klimova, S. Zherebtsov, A. Efimov, G. Salishchev, Effect of cryo-deformation on structure and properties of CoCrFeNiMn high-entropy alloy, *Intermetallics*. 59 (2015) 8–17.
- [20] B. Schuh, F. Mendez-Martin, B. Völker, E.P. George, H. Clemens, R. Pippan, A. Hohenwarter, Mechanical properties, microstructure and thermal stability of a nanocrystalline CoCrFeMnNi high-entropy alloy after severe plastic deformation, *Acta Mater.* 96 (2015) 258–268.
- [21] S.A. Humphry-Baker, C.A. Schuh, Suppression of grain growth in nanocrystalline Bi2Te3 through oxide particle dispersions, *J. Appl. Phys.* 116 (17) (2014), 173505.
- [22] A.A. Kaminskii, M.S. Akchurin, R.V. Gainutdinov, K. Takaichi, A. Shirakava, H. Yagi, T. Yanagitani, K. Ueda, Microhardness and fracture toughness of Y2O3- and Y3Al5O12-based nanocrystalline laser ceramics, *Crystallogr. Rep.* 50 (5) (2005) 869–873.
- [23] N.D. Stepanov, D.G. Shaysultanov, G.A. Salishchev, M.A. Tikhonovsky, E. E. Oleynik, A.S. Tortika, O.N. Senkov, Effect of V content on microstructure and mechanical properties of the CoCrFeMnNi_x high entropy alloys, *J. Alloys Compd.* 628 (2015) 170–185.
- [24] G. Qin, Z.B. Li, R.R. Chen, H.T. Zheng, C.L. Fan, L. Wang, Y.Q. Su, H.S. Ding, J. J. Guo, H.Z. Fu, CoCrFeMnNi high-entropy alloys reinforced with Laves phase by adding Nb and Ti elements, *J. Mater. Res.* 34 (2019) 1011–1020.
- [25] A. Takeuchi, A. Inoue, Classification of bulk metallic glasses by atomic size difference, heat of mixing and period of constituent elements and its application to characterization of the main alloying element, *Mater. Trans.* 46 (2005) 2817–2829.
- [26] Y.H. Liang, C.L. Li, C.H. Hsueh, Effects of Nb Addition on Microstructures and Mechanical Properties of Nb_x-CoCrFeMnNi High Entropy Alloy Films, *Coatings* 11 (2021) 1539.
- [27] T. Nagase, P.D. Rack, J.H. Noh, T. Egami, Dynamic strain aging of Al0.3CoCrFeNi high entropy alloy single crystals, *Intermetallics* 59 (2015) 32.
- [28] I. Toda-Caraballo, P.E.J. Rivera-Díaz-del-Castillo, Modelling solid solution hardening in high entropy alloys, *Acta Mater.* 85 (2015) 14.
- [29] S.Q. Xia, X. Yang, T.F. Yang, Irradiation Resistance in Al x CoCrFeNi High Entropy Alloys, *JOM* 67 (2015) 2340–2344.
- [30] T.J. Novakowski, J.K. Tripathi, A. Hassanein, Effect of high-flux, low-energy He+ ion irradiation on Ta as a plasma-facing material, *Sci. Rep.* 6 (2016) 39746.

- [31] Z. Fan, W. Zhong, K. Jin, H. Bei, Y.N. Ostesky, Y. Zhang, Diffusion-mediated chemical concentration variation and void evolution in ion-irradiated NiCoFeCr high-entropy alloy, *J. Mater. Res.* 36 (2021).
- [32] E.J. Pickering, A.W. Carruthers, P.J. Barron, S.C. Middleburgh, D.E.J. Armstrong, A.S. Gandy, High entropy alloys for advanced nuclear application, *Entropy (Basel)* 23 (1) (2021) 98.
- [33] G.S. Was, S.J. Zinkle, Toward the Use of Ion Irradiation to Predict Reactor Irradiation Effects, Reference Module in Materials Science and Materials Engineering, In book, 2020.
- [34] N.W. Phillips, H. Yu, S. Das, D. Yang, K. Mizohata, W. Liu, R. Xu, R.J. Harder, F. Hofmann, Nanoscale lattice strains in self-ion implanted tungsten, *Acta Mater.* 195 (2020) 219–228.
- [35] D.R. Mason, X. Yi, M.A. Kirk, S.L. Dudarev, Elastic trapping of dislocation loops in cascades in ion-irradiated tungsten foils, *J. Phys. Cond. Matter* 26 (2014), 375701.
- [36] A.E. Sand, K. Nordlund, S.L. Dudarev, Radiation damage production in massive cascades initiated by fusion neutrons in tungsten, *J. Nucl. Mater.* 455 (1–3) (2014) 207–211.
- [37] K. Mergia, N. Boukos, Structural, thermal, electrical and magnetic properties of Eurofer 97 steel, *J. Nucl. Mater.* 373 (1–3) (2008) 1–8.
- [38] H. Hadraha, Z. Chlupá, A. Dlouhy, F. Dobes, P. Roupcova, M. Vilemova, J. Matejicek, Oxide dispersion strengthened CoCrFeNiMn high-entropy alloy, *Mater. Sci. Eng. A* 689 (2017) 252–256.
- [39] J. F. Ziegler et al., SRIM: The stopping and range of ions in matter, Version SRIM-2013. <http://www.srim.org/>.
- [40] E. Stoller, M.B. Toloczo, G.S. Was, A.G. Certain, S. Dwaraknath, F.A. Garner, On the use of SRIM for computing radiation damage exposure, *Nucl. Instrum. Methods Phys. Res. B* 310 (2013) 75–80.
- [41] ASTM E521, 96(2009) Standard practice for neutron irradiation damage simulation by charged particle irradiation, Annual Book of ASTM Standards, Vol. 12.02, ASTM International, West Conshohocken, PA, 2009.
- [42] P. Jung, Production of atomic defects in metals by irradiation. in *Atomic Defects in Metals* (ed. Ullmaier, H.) 25, 6–7 (Springer-Verlag, 1991).
- [43] A.Y. Konobeyev, U. Fischer, Y.A. Korovin, S.P. Simakov, Evaluation of effective threshold displacement energies and other data required for the calculation of advanced atomic displacement cross-sections, *Nucl. Energy Technol.* 3 (2017) 169–175.
- [44] R. Krause-Rehberg, H.S. Leipner, Positron annihilation in semiconductors: defect studies, 1999.
- [45] F. Tuomisto, I. Makkonen, Defect identification in semiconductors with positron annihilation: Experiment and theory, *Rev. Mod. Phys.* 85 (2013) 1583–1631.
- [46] M.O. Liedke, W. Anwand, R. Bali, S. Cornelius, M. Butterling, T.T. Trinh, A. Wagner, S. Salamon, D. Walecki, A. Smekhova, H. Wende, K. Potzger, Open volume defects and magnetic phase transition in Fe 60 Al 40 transition metal aluminide, *J. Appl. Phys.* 117 (2015), 163908.
- [47] W. Anwand, G. Brauer, M. Butterling, H.R. Kissener, A. Wagner, Design and Construction of a Slow Positron Beam for Solid and Surface Investigations, *Defect Diffus. Forum.* 331 (2012) 25–40.
- [48] J. Dryzek, P. Horodek, GEANT4 simulation of slow positron beam implantation profiles, *Nucl. Instruments Methods Phys. Res. Sect. B Beam Interact. with Mater. Atoms.* 266 (2008) 4000–4009.
- [49] A. Wagner, W. Anwand, A.G. Attallah, G. Dornberg, M. Elsayed, D. Enke, A.E. M. Hussein, R. Krause-Rehberg, M.O. Liedke, K. Potzger, T.T. Trinh, Positron annihilation lifetime spectroscopy at a superconducting electron accelerator, *J. Phys. Conf. Ser.* 791 (2017), 012004.
- [50] A. Wagner, M. Butterling, M.O. Liedke, K. Potzger, R. Krause-Rehberg, Positron annihilation lifetime and Doppler broadening spectroscopy at the ELBE facility, *AIP Conf. Proc.* 040003 (2018).
- [51] J.V. Olsen, P. Kirkegaard, N.J. Pedersen, M. Eldrup, PALSfit: A new program for the evaluation of positron lifetime spectra, *Phys. Status Solidi.* 4 (2007) 4004–4006.
- [52] E.H. Khan, M.H. Weber, M.D. McCluskey, Formation of Isolated Zn Vacancies in ZnO Single Crystals by Absorption of Ultraviolet Radiation: A Combined Study Using Positron Annihilation, Photoluminescence, and Mass Spectroscopy Phys., *Rev. Lett.* 111 (2013), 017401.
- [53] J. Martan, O. Herve, V. Lang, Two-detector measurement system of pulse photothermal radiometry for the investigation of the thermal properties of thin films, *J. Appl. Phys.* 102 (2007), 064903.
- [54] J. Martan, Optical layer development for thin films thermal conductivity measurement by pulsed photothermal radiometry, *Rev. Sci. Instrum.* 86 (2015), 014902.
- [55] D.L. Balageas, J.C. Krapez, P. Cielo, Pulsed photothermal modelling of layered materials, *J. Appl. Phys.* 59 (1986) 348.
- [56] M. J. Riedl, Optical design fundamentals for infrared systems, in: *SPIE Press Book*, Washington, 2001.
- [57] N. Gayathri, P. Mukherjee, S. Mandal, A. Sarkar, U. Saha, S. Dey, A. Dutta, T. K. Roy, S. Neogy, Post irradiated microstructure and mechanical properties of pure V, *J. Nucl. Mater.* 564 (2022), 153648.
- [58] M.A. Tagliente, M. Massaro, Strain-driven (0 0 2) preferred orientation of ZnO nanoparticles in ion-implanted silica, *Nucl. Instrum. Methods Phys. Res. B* 266 (2008) 1055–1061.
- [59] W.C. Oliver, G.M. Pharr, An improved technique for determining hardness and elastic modulus using load and displacement sensing indentation experiments, *J. Mater. Res.* 7 (1992) 1564–1583.
- [60] A. Macková, S. Fernandes, J. Matejíček, M. Vilémová, V. Holý, M.O. Liedke, J. Martan, M. Vronka, M. Potoček, P. Bábor, M. Butterling, A.G. Attallah, Radiation damage evolution in pure W and W-Cr-Hf alloy caused by 5 MeV Au ions in a broad range of dpa, *Nucl. Mater. Energy* 29 (2021), 101085.
- [61] D. Hyeon-Seok, L. Byeong-Joo, Origin of radiation resistance in multi-principal element alloys, *Sci. Rep.* 8 (2018) 16015.
- [62] S. Agarwal, M.O. Liedke, A.C.L. Jones, E. Reed, A.A. Kohnert, B.P. Überuaga, Y.Q. Wang, J. Cooper, D. Kaoumi, N. Li, R. Auguste, P. Hosemann, L. Capolungo, D. J. Edwards, M. Butterling, E. Hirschmann, A. Wagner, F.A. Selim, A new mechanism for void-cascade interaction from nondestructive depth-resolved atomic-scale measurements of ion irradiation-induced defects in Fe, *Sci. Adv.* 6 (2020) eaba8437.
- [63] S. Agarwal, M. Butterling, M.O. Liedke, K.H. Yano, D.K. Schreiber, A.C.L. Jones, B. P. Überuaga, Y.Q. Wang, M. Chancey, H. Kim, B.K. Derby, N. Li, D.J. Edwards, P. Hosemann, D. Kaoumi, E. Hirschmann, A. Wagner, F.A. Selim, The mechanism behind the high radiation tolerance of Fe–Cr alloys, *J. Appl. Phys.* 131 (2022), 125903.
- [64] J. Čížek, O. Melikhova, Z. Barnovská, I. Procházka, R.K. Islamgaliev, Vacancy clusters in ultra fine grained metals prepared by severe plastic deformation, *J. Phys. Conf. Ser.* 443 (2013), 012008.
- [65] M. Elsayed, R. Krause-Rehberg, C. Eischenmidt, N. Eißmann, B. Kieback, Defect Study in CoCrFeMnNi High Entropy Alloy by Positron Annihilation Lifetime Spectroscopy, *Phys. Status Solidi.* 215 (2018) 1800036.
- [66] O. El-Atwani, E. Esquivel, M. Efe, E. Aydogan, Y.Q. Wang, E. Martinez, S.A. Maloy, Loop and void damage during heavy ion irradiation on nanocrystalline and coarse grained tungsten: Microstructure, effect of dpa rate, temperature, and grain size, *Acta Mater.* 149 (2018) 206–219.
- [67] M.A. Cusentino, M.A. Wood, R. Dingreville, Compositional and structural origins of radiation damage mitigation in high-entropy alloys, *J. Appl. Phys.* 128 (2020), 125904.
- [68] D. Choi, The electron scattering at grain boundaries in tungsten films, *Microelectron. Eng.* 122 (5) (2014) 5–8.
- [69] D.L. Balageas, J.C. Krapez, P. Cielo, Pulsed photothermal modeling of layered materials, *J. Appl. Phys.* 59 (1986) 348.
- [70] Y. Zhang, G.M. Stocks, K. Jin, C. Lu, H. Bei, B.C. Sales, L. Wang, L.K. Beland, R. E. Stoller, G.D. Samolyuk, M. Caro, A. Caro, W.J. Weber, Influence of chemical disorder on energy dissipation and defect evolution in concentrated solid solution alloys, *Nat. Commun.* 6 (2015) 8736.